A high-resolution benthic stable-isotope record for the South Atlantic: implications for orbital-scale changes in Late Paleocene – Early Eocene climate and carbon cycling

Kate Littler[a,1*]; Ursula Röhl[b]; Thomas Westerhold[b]; James C. Zachos[a]

[a]Department of Earth and Planetary Sciences, University of California Santa Cruz, 1156 High Street, Santa Cruz, CA 95064, USA.

[b]MARUM, University of Bremen, Leobener Strasse, 28359 Bremen, Germany

[1]Present address for K.L: Camborne School of Mines, University of Exeter, Penryn, Cornwall, TR10 9FE, UK

*Corresponding author

Email: *k.littler@exeter.ac.uk; uroehl@marum.de; twesterhold@marum.de; jzachos@ucsc.edu

Keywords: Paleogene, paleoclimate, carbon isotopes, oxygen isotopes, benthic foraminifera, Milankovitch cycles, orbital forcing, cyclostratigraphy, hyperthermals, PETM, Ocean Drilling Program

Abstract

The Late Paleocene and Early Eocene were characterised by warm greenhouse climates, punctuated by a series of rapid warming and ocean acidification events known as "hyperthermals", thought to have been paced or triggered by orbital cycles. While these hyperthermals, such as the Paleocene Eocene Thermal Maximum (PETM), have been studied in great detail, the background low-amplitude cycles seen in carbon and oxygen-isotope records throughout the Paleocene–Eocene have hitherto not been resolved. Here we present a 7.7 million year (myr) long, high-resolution, orbitally-tuned, benthic foraminiferal

stable-isotope record spanning the late Paleocene and early Eocene interval (~52.5 – 60.5 Ma) from Ocean Drilling Program (ODP) Site 1262, South Atlantic. This high resolution (~2–4 kyr) record allows the changing character and phasing of orbitally-modulated cycles to be studied in unprecedented detail as it reflects the long-term trend in carbon cycle and climate over this interval. The main pacemaker in the benthic oxygen-isotope ($\delta^{18}O$) and carbon-isotope ($\delta^{13}C$) records from ODP Site 1262, are the long (405 kyr) and short (100 kyr) eccentricity cycles, and precession (21 kyr). Obliquity (41 kyr) is almost absent throughout the section except for a few brief intervals where it has a relatively weak influence. During the course of the Early Paleogene record, and particularly in the latest Paleocene, eccentricity-paced negative carbon-isotope excursions ($\delta^{13}C$, CIEs) and coeval negative oxygen-isotope ($\delta^{18}O$) excursions correspond to low carbonate ($CaCO_3$) and coarse fraction (%CF) values due to increased carbonate dissolution, suggesting shoaling of the lysocline and accompanied changes in the global exogenic carbon cycle. These negative CIEs and $\delta^{18}O$ events coincide with maxima in eccentricity, with changes in $\delta^{18}O$ leading changes in $\delta^{13}C$ by ~6 (±5) kyr in the 405-kyr band and by ~3 (±1) kyr in the higher frequency 100-kyr band on average. However, these phase lags are not constant, with the lag in the 405-kyr band extending from ~4 (±5) kyr to ~21 (±2) kyr from the late Paleocene to the early Eocene, suggesting a progressively weaker coupling of climate and the carbon-cycle with time. The higher amplitude 405-kyr cycles in the latest Paleocene are associated with changes in bottom water temperature of 2–4ºC, while the most prominent 100 kyr-paced cycles can be accompanied by changes of up to 1.5ºC. Comparison of the 1262 record with a lower resolution, but orbitally-tuned benthic record for Site 1209 in the Pacific allows for verification of key features of the benthic isotope records which are global in scale including a key warming step at 57.7 Ma.

53 **1. Introduction**

54

55 The Early Paleogene was climatically dynamic, with both sustained and transient
56 episodes of elevated global temperatures and pCO_2 levels, as well as periodic carbon-cycle
57 and climatic perturbations of varying magnitude. This period, therefore, provides a diversity
58 of case studies for investigating the links between orbital forcing, climate and the carbon-
59 cycle under a range of greenhouse conditions, and for determining the role of threshold
60 events in the climate system in response to gradual changes in boundary conditions. This
61 period is marked by long-term warming from the mid Paleocene (~58 Ma) to the Early
62 Eocene, culminating in the Early Eocene Climatic Optimum (EECO, ~51 Ma) when global
63 temperatures were the warmest of the past 90 myr (Zachos et al., 2001; Friedrich et al 2012).
64 This change from a relatively cool Paleocene to a very warm Early Eocene is expressed in a
65 decrease of global benthic $\delta^{18}O$ values of >1 ‰ over ~9 myr, representing a change in
66 bottom water temperatures on the order of ~6°C (Zachos et al., 2001). The early Paleogene
67 carbon-cycle was also very dynamic, with long-term swings in the benthic carbon-isotope
68 record ($\delta^{13}C$) on the order of ±2.5 ‰ (Zachos et al., 2008).

69 Superimposed on these long-term climate and carbon-cycle trends were a series of
70 high-amplitude, transient perturbations to the climate and carbon-cycle known as
71 "hyperthermals", the largest and best-studied of which is the Paleocene Eocene Thermal
72 Maximum (PETM; ETM-1; ~55.5 Ma) (e.g., Kennett and Stott, 1991; Zachos et al., 2005;
73 Lourens et al., 2005; Röhl et al., 2007; Tripati and Elderfield 2005; Sluijs et al., 2006; 2007;
74 Röhl et al., 2007; Nicolo et al. 2007; McInerney and Wing, 2011). At least three such
75 hyperthermals are recognised in the Early Eocene (ETM-1 to 3), which all share similar
76 characteristics of rapid and large increases in global temperature accompanied by transient
77 changes to the global carbon-cycle, as recorded by negative excursions in $\delta^{18}O$ and $\delta^{13}C$

78 records, and evidence for massive dissolution of deep-sea marine carbonates (e.g., Zachos et
79 al., 2005; Lourens et al., 2005; Sluijs et al., 2009; Agnini et al., 2009; Stap et al., 2009;
80 2010a,b; McInerney and Wing, 2011, Komar et al., 2013). Similar events, of smaller
81 magnitude have also been recorded from the Paleocene (e.g., Top C27n event, aka the LDE
82 (Latest Danian Event), Dan C2 event, the Early Late Paleocene Event (ELPE) etc; Röhl et
83 al., 2004; Westerhold et al., 2011; Coccioni et al., 2010; Quillévéré et al., 2008), as well as
84 lower amplitude cyclic perturbations, particularly in the latest Paleocene (Cramer et al.,
85 2003; Zachos et al., 2010). Construction of orbitally-tuned age models for the Early
86 Paleogene events suggests that many if not all of the hyperthermals, and many of the other
87 smaller perturbations during this interval, were paced by variations in Earth's orbit, with
88 particular power in the long (405 kyr) and short (100 kyr) eccentricity bands (e.g., Lourens
89 et al., 2005; Westerhold et al., 2007; 2008; Zachos et al., 2010; Hilgen et al., 2010; Galeotti
90 et al., 2010).
91 The causal mechanism for the initiation of the large hyperthermals such as the PETM
92 remains contentious, with the leading hypothesis involving the release of large quantities of
93 reduced carbon from methane clathrate reservoirs (Dickens 1995, 1997; Zeebe et al., 2009).
94 A mechanism to initiate release of this methane is still a matter of debate (e.g., Sluijs et al.,
95 2007), but several triggers have been suggested, including: the crossing of a climatic
96 threshold associated with the long-term warming trend (Lourens et al., 2005, Lunt et al,
97 2010, DeConto et al, 2012), or a pulse of NAIP volcanism that caused warming above the
98 background values or release of thermogenic methane (Svensen et al., 2004; Storey et al.,
99 2007; Wieczorek et al., 2013; Rampino, 2013). Other theories put forward to explain the
100 origin of the hyperthermals include the large-scale release of Antarctic permafrost carbon
101 due to favourable orbital configurations (DeConto et al, 2012), desiccation of a large marine
102 basin (Higgins and Schrag 2006), or even a cometary impact (Kent et al., 2003), of which

103 the latter two seem unlikely due to a lack of evidence or a mechanism linking orbital
104 cyclicity with these phenomenon.
105 While the highest amplitude hyperthermals have been studied in great detail and with
106 various multi-proxy and modelling approaches, the preceding and intervening millions of
107 years have thus far largely been constrained by lower-resolution, often composite, datasets,
108 which provide insufficient resolution to ascertain the forcing behind the high-frequency
109 variations in climate and the carbon-cycle, at least of the extent that they have been resolved
110 (e.g., Zachos et al., 2001; Cramer et al., 2003; Zachos et al., 2010). In particular, the existing
111 benthic stable-isotope record for the early Paleogene is composed of stacked records from
112 many different deep-sea sites, and from various ocean basins (e.g. Zachos et al., 2001, and
113 references therein). While useful for some applications, the stacked records lack the fidelity
114 required to resolve climate and carbon cycle variations on orbital frequencies, and therefore
115 to ascertain the true nature of the hyperthermals and other transient climate phenomena of
116 the Paleogene. Arguably, resolution of the higher frequency patterns of paleoceanographic
117 variability is also essential to resolving the origin of the long-term trends.
118 Here we present a stratigraphically continuous, high-resolution benthic foraminiferal
119 stable-isotope record from ODP Site 1262 in the South Atlantic, which encompasses almost
120 8 myr of astronomically-tuned time spanning the Late Paleocene to Early Eocene (C24.2r to
121 C26r). This complements and extends a shorter, high-resolution bulk stable-isotope record
122 from Site 1262 (Zachos et al., 2010). Comparison of the new Atlantic isotopic record to a
123 corresponding benthic stable-isotope record from the Pacific allows for isolation of the
124 global from local signals (Westerhold et al., 2011). We then explore the implications of
125 these records for the long-term evolution of the climate and marine carbon cycle response to
126 orbital forcing over the late Paleocene-early Eocene as the planet slowly warmed.
127

2. Materials and methods

2.1. Site location, lithology and sampling

ODP Site 1262 is located in the eastern South Atlantic (27°S) at a water depth of 4759 m, and is the deepest site drilled as part of the Leg 208 Walvis Ridge depth transect (Zachos et al., 2004). This site was located at a paleolatitude of ~34°S in the Paleogene (Fig 1). Three offset holes (A, B, C) were cored using advanced piston coring (APC) system ensuring complete recovery of the section with minimal coring disturbance. Shipboard splices of the holes was achieved using magnetic susceptibility data (Zachos et al., 2004) and later confirmed using high resolution XRF scanning Fe data (Westerhold et al., 2007, 2008). Early Paleogene sediments at Site 1262 predominantly consist of nannofossil oozes with fluctuating proportions of clay and variable preservation of carbonate microfossils, indicative of deposition above, but close to, a dynamic lysocline, at a paleodepth of ~3600 m (Zachos et al., 2004). Samples were taken from both Holes 1262A and 1262B. Samples were taken every 3 cm of the splice from Holes 1262A and 1262B between 109 and 185 mcd. According to the adopted chronology (see below), this implies a temporal resolution of ~2.5 kyr for much of the Latest Paleocene–Earliest Eocene (114–165 mbsf), and a slightly lower resolution ~3–4.5 kyr in the mid Late Paleocene (165–185 mbsf), and the post-ETM-2 Early Eocene interval (109–114 mbsf). Freeze-dried samples were soaked in distilled water to disaggregate, then washed through a 38 μm mesh sieve and rinsed with ethanol before being dried. Benthic stable-isotope data was generated from 2714 samples of the cosmopolitan deep-water benthic foraminifera *Nuttalides truempyi* picked from the >150 μm fraction (1900 at Santa Cruz and 814 at MARUM, Bremen).

2.2. Stable isotopes

On average, 11 specimens of *N. truempyi* were used for each isotopic analysis. Isotopic measurements were carried out on a Thermo-Finnigan MAT253 mass spectrometer interfaced with a Kiel Device (UCSC), and a Thermo-Finnigan MAT251 mass spectrometer interfaced with a Kiel Device (MARUM, Bremen). At UCSC, analytical precision (1σ) is based on repeat analysis of an in-house standard (Carrara marble), calibrated to the international standards NBS18 and NBS19, and averages ±0.05 ‰ for $\delta^{13}C$ and ±0.08 ‰ for $\delta^{18}O$. At Bremen, analytical precision (1σ) is based on the in-house standard (Solnhofen Limestone) also calibrated to the international standard NBS19, and averages 0.05 ‰ for $\delta^{13}C$ and 0.07 ‰ for $\delta^{18}O$. All values are reported relative to VPDB. Additionally, 840 new samples from the mid-Late Paleocene (159–185 mcd) were analyzed at the MARUM to generate a new bulk $\delta^{13}C$ record, to compliment the existing Late Paleocene–Early Eocene bulk data from Zachos et al. (2010). The complete data set is available online in the PANGAEA database *doiXXXXX [To be uploaded upon publication*].

Conversions of benthic $\delta^{18}O$ to temperature are made using Equation 1 of Bemis et al. (1998) with modifications to adjust *N. truempyi* values to *Cibicidoides* values after Katz et al. (2003) (Eq. 1), and assuming an ice-free $\delta^{18}O_{sw}$ value of -1.2 ‰ (VPDB). However, all isotope data presented in the figures herein are plotted as the original, uncorrected data relative to VPDB.

Eq. 1 $$\delta^{18}O_{Cib} = (\delta^{18}O_{Nutt} + 0.10) / 0.89$$

Where $\delta^{18}O_{Nutt}$ is the measured $\delta^{18}O$ value of the analysed *N. truempyi* specimens, and $\delta^{18}O_{cib}$ is the corrected *Cibicidoides* equivalent value, both relative to VPDB.

2.3. Coarse Fraction

The wt % Coarse Fraction (%CF) is defined as the weight of the >38 μm fraction in each sample, divided by the dry weight of whole rock sample prior to sample processing,

and provides a semi-quantitative measure of the degree of carbonate dissolution during and immediately after deposition. At Site 1262, this fraction is composed primarily of planktonic foraminifer shells, which range from intact to fragmented, with a larger proportion of the former relative to the latter.

2.4. Chronology, data filtering and time series analysis

The age model for Site 1262 is based on recognition of the stable long-eccentricity (405 kyr) cycle observed in XRF scanning Fe concentration data, reaching from the K-Pg boundary into the Early Eocene (Westerhold et al., 2007; 2008). Published biostratigraphic and magnetostratigraphic information was integrated with this cycle-counting method to confer a fully integrated orbitally-tuned chronology for this site. All absolute ages herein are based on tuning option 1 of Westerhold et al. (2008), to the orbital solution of Laskar et al. (2004). This existing age model has been marginally extended for the youngest part of the study interval, to include a new orbitally-tuned chronology for the Early Eocene encompassing $Eccentricity_{100}$ cycles 28 –32 (~52.9–52.5 Ma). The extension of the age model has no effect on the conclusions in this paper as it merely builds upon the existing methodology from Westerhold et al. (2008), and no comparison is made with records from other sites for this time interval. It should be noted that an alternative age model has been proposed by Hilgen et al. (2010) for the Paleocene. This model is also based on recognition of the stable 405-kyr cycle and is consistent with Westerhold et al., (2008) in the interval presented here, therefore, the lead/lag relationships discussed below will be the same regardless of the age model applied.

Time series analysis and data filtering were performed on the orbitally-tuned isotopic and %CF records, to ascertain the dominant response of climate and the carbon-cycle to orbital forcing during the Paleocene–Eocene. Prior to analysis, all obvious outliers (e.g., single data points with values that differed >0.5 ‰ from adjacent data points) were

removed, along with the main body of the PETM (from initiation through the majority of the recovery period; ~55.4–55.5 Ma), to reduce the distorting effects these can have on spectral analysis results. A linear interpolation across the PETM was used to replace the hyperthermal interval. The records were then detrended graphically (KaleidaGraph 4.0) using a 15% running mean to remove the very long-term trends. The data were then cropped, such that all detrended $\delta^{13}O$ data <-0.6 and >0.4 and all detrended $\delta^{18}O$ data <-0.4 and >0.3 ‰, were removed. The time series were then linearly resampled at 3 kyr intervals (AnalySeries 2.0 (Paillard et al., 1996)). Band pass filtering was conducted using AnalySeries 2.0 for the 405-kyr eccentricity at 0.002467 ± 0.0007 cycles/kyr (i.e., 565–316 kyr), 100-kyr eccentricity at 0.01 ± 0.003 (i.e., 77–143 kyr), and ~21 kyr precession at 0.0476 ± 0.0143 (16–30 kyr). Cross-spectral analysis to determine the coherency and phasing between the oxygen- and carbon-isotope records was performed using the Blackman-Tukey cross-spectral analysis in AnalySeries. Error bars on figures represent 97.5% CI values. MTM power spectra were generated using the kSpectra Toolkit using three tapers and a resolution of 2, where background estimate and therefore confidence levels (90%, 95%, and 99%) are based on a red noise estimation (Mann and Lees, 1996). Evolutionary wavelet spectra were obtained using software provided by C. Torrence and G. Compo (http://paos.colorado.edu/research/wavelets).

3. Results

3.1. Foraminiferal preservation

Preservation of *Nuttalides truempyi* was generally very good to good throughout the record, particularly in the earliest Eocene. All picked specimens appeared well preserved,, with minimal signs of diagenetic overgrowth or infilling with secondary calcite. As

226 expected, throughout the record %CF and foraminiferal preservation tended to covary,
227 whereby foraminifera from intervals with lower %CF showed signs of poorer preservation
228 (i.e., signs of dissolution to the surface of the tests).

229 **3.2. Long-term trends in the new stable-isotope and coarse fraction records**

230 The 7.7 myr long bulk and benthic stable-isotope record, along with %CF and Fe
231 data (Westerhold et al., 2007), is plotted against age in Fig. 2 and against depth in Fig. S1.
232 The broad-scale trends in the benthic $\delta^{13}C$ record largely follow those known from the
233 stacked benthic $\delta^{13}C$ record (Zachos et al., 2008), including the PCIM and the long-term
234 decline of values into the early Eocene. The finer-scale trends in the benthic $\delta^{13}C$ record are
235 paralleled by trends in the bulk $\delta^{13}C$ record, albeit offset by ~1–1.5 ‰ throughout much of
236 the record (Fig. 2). The only discrepancy is near the crest of the Paleocene Carbon Isotope
237 Maximum (PCIM; ~57.7 Ma), where a modest positive excursion in bulk $\delta^{13}C$ values is
238 expressed as a much larger amplitude step in the corresponding benthic record (Figs. 2, S2).
239 The long-term decrease in $\delta^{18}O$ values from the Late Paleocene to the Early Eocene
240 associated with global warming, and well-known from the stacked benthic record (Zachos et
241 al., 2008), can clearly be seen in the new single-site Site 1262 benthic record (Fig. S4). The
242 exceptions are a large negative excursion in values associated with the late Paleocene ELPE
243 (~58.9 Ma; Fig. S2b), and a ~3°C cooling event between ~54.5 and 55 Ma, prior to the
244 resumption of the long-term warming trend (Fig. S3). As in all carbonate-rich pelagic
245 sediments, the bulk sediment oxygen isotope record is overprinted by recrystallization,
246 which, at shallow burial depths and near seafloor temperatures, typically shifts the mean
247 bulk $\delta^{18}O$ values toward benthic values (Schrag et al., 1995; Fig. S4).
248 The %CF record also shows a long-term evolution in baseline values that can be
249 correlated with the sedimentation rate and with long-term trends in the benthic and bulk
250 $\delta^{13}C$ records. Generally low %CF values in the late Paleocene, pass through a period of

variable and fluctuating values in the latest Paleocene, before becoming significantly higher in the earliest Eocene (Figs. 2, S1).

3.3. Orbital cyclicity

In addition to the long-term evolution in climate and the carbon-cycle documented in the benthic stable-isotope and %CF records, variability associated with orbital forcing is prominent throughout this 7.7 myr interval. Spectral analysis of the data using band-pass filtering (Fig. 3), MTM power spectrum analysis (Fig. 4), and evolutive wavelet analysis (Fig. 5) all show that eccentricity is the dominant pacemaker of both the isotopic and %CF records, consistent with observations based on the original shipboard magnetic susceptibility data (Zachos et al., 2004; Lourens et al., 2005, high-resolution Fe intensity data (Westerhold et al., 2007; 2008) and the existing bulk $\delta^{13}C$ record (Zachos et al., 2010). The long eccentricity cycle (405 kyr) is the strongest frequency throughout, with the largest changes in benthic $\delta^{13}C$ and $\delta^{18}O$ values, but power is also concentrated in the short eccentricity (~100 kyr) band, with many of the largest amplitude and most abrupt CIEs occurring in association with this shorter cycle (e.g., the ETM2, H2, I1, D2, C2 etc; Fig. 2). The resolution and length of the new isotopic records allows the split peak of the short eccentricity bands to be resolved, with distinctive peaks in spectral power at ~125 and 95 kyr in both $\delta^{13}C$ and $\delta^{18}O$ (Fig. 4). The high-resolution nature of the new Site 1262 records means that it is also possible to resolve precession (~21 kyr), which occurs as a prominent frequency in both the benthic $\delta^{18}O$ and $\delta^{13}C$ records (Figs. 3, 4). Power in the obliquity band (~41 kyr) is weak throughout the Late Paleocene–Early Eocene in all of the records.

The influence of the various orbital cycles changes with time, with long and short eccentricity being most dominant in the Latest Paleocene (~56–57.5 Ma), and the Early Eocene (52.5–55 Ma) associated with large amplitude swings in both $\delta^{13}C$ and $\delta^{18}O$ values (Figs. 3, 5). Across some of the largest of these Paleocene 405-kyr cycles (e.g. B2–C2) the

equivalent of 2–4ºC in bottom water temperature change occurs between eccentricity minima and maxima, while some of the largest 100 kyr-paced events, such as D2, are associated with changes in bottom water temperature of ~1.5ºC (Fig. 2, S5). The influence of the 405-kyr cycle is weakest in the Late Paleocene prior to 57.7 Ma, and in the earliest Eocene in the immediate post-PETM interval, where power in the long eccentricity band is anomalously low despite persistent power in the short-eccentricity band (~100 kyr) (Figs. 3, 6).

Cross-spectral analysis of the benthic stable-isotope records suggests that climate and the carbon-cycle are highly coherent on orbital timescales, particularly so in the eccentricity and precession bands (Fig. 6). Over the whole record, changes in bottom water temperature ($\delta^{18}O$) appear to lead changes in the carbon-cycle ($\delta^{13}C$) in the eccentricity bands, with an average lag of ~6 (±5) kyr at the 405-kyr frequency, and ~3 (±1) kyr at the 100-kyr band (Fig. 6, Table S1). Closer inspection of the phase relationships through time reveals that these lags are not constant throughout the entire 7.7 myr long record (Fig. S6, Table S2), although care must be taken in interpreting changes in apparent phasing using cross-spectral analysis, as during low-amplitude cycles in the isotopic records (e.g., 58–59 Ma) the relative phasing can be difficult to determine. At the 405-kyr frequency the lag between climate and the carbon-cycle response is least conspicuous in the Late Paleocene, averaging only ~4 (±5) kyr, but extends to an average of ~21 (±2) kyr in the Early Eocene, post-ETM-2. The 23 and 19 kyr precessional components of both isotopic time series are close to being in-phase throughout, with $\delta^{18}O$ leading or lagging by only 1– 2 kyrs (Fig. S6). By contrast, cross-spectral analysis of the %CF and benthic $\delta^{13}C$ records suggest that these records are less coherent, but that the former often leads the latter at principle orbital frequencies by 2–20 kyrs (Figs. 6, S7, Tables S1, S2).

4. Discussion

The new benthic stable-isotope record from ODP Site 1262 is the longest, stratigraphically continuous, high-resolution record of its kind for the Late Paleocene–Early Eocene interval in the Atlantic. This unique record resolves both long-term trends in climate and the carbon-cycle, and short-term orbitally-paced variation.

4.1. Long-term trends in Paleogene climate and carbon-cycling

4.1.1. Inferences from the new benthic stable-isotope record

Comparison of the Site 1262 benthic stable-isotope record to the existing North Pacific record from ODP Site 1209 (Westerhold et al., 2011) reveals remarkably close correlation between benthic $\delta^{18}O$ at the two sites, thus indicating relatively uniform bottom water temperature between deep basins throughout the late Paleocene and early Eocene on long and short-time scales (Fig. 7). The long-term warming trend over this time, was likely driven by greenhouse forcing from periodic outgassing of volcanogenic CO_2 from the North Atlantic Igneous Province (NAIP), which was active throughout the latest Paleocene–earliest Eocene from ~62 to ~52 Ma (e.g., Sinton and Duncan, 1998; Saunders et al., 1997; 2007, Storey et al. 2007). The second phase of NAIP activity, which initiated at ~57.5 Ma and was associated with extensive rifting and crustal extension in the North Atlantic, was vigorous and likely led to the emplacement of significant quantities of new crustal material and large subsequent volcanic emissions (Sinton and Duncan, 1998; Saunders et al., 1997). The beginning of this phase coincides with the relatively rapid initiation of the deep-sea warming trend seen in both the Atlantic (Site 1262) and the Pacific (Site 1209), suggesting both that the onset of volcanism was relatively abrupt and that sufficient volumes of volcanic CO_2 accumulated in the atmosphere over millions of years to sustain increasing global temperatures into the Early Eocene (Fig. 7; Arthur, 1980; Corfield and Cartlidge, 1992; Zachos et al., 2008; Westerhold et al., 2011).

In the Late Paleocene, prior to the initiation of the warming trend, $\delta^{13}C$ values at Sites 1263 and 1209 increased to the most positive values of the Cenozoic, forming the broad peak of the PCIM (~57–58 Ma) (Fig. 2). The relatively cool greenhouse conditions of the latest Paleocene (~63–59 Ma) likely facilitated the accumulation of carbon in reduced reservoirs such as methane hydrates, peat, and/or permafrost, which led to a net positive shift in the residual oceanic $\delta^{13}C$ budget (Shackleton et al., 1984; Shackleton, 1986; Corfield and Cartlidge, 1992; Corfield 1996; Kalkreuth, 2004). This large-scale carbon burial also likely led to the drawdown of atmospheric CO_2, which corresponds with benthic $\delta^{18}O$ evidence for a global cooling at this time (Zachos et al., 2008; Fig. 2). Evidence from sulphur isotopes and the large coal reserves of Late Paleocene age, suggests a large proportion of this massive organic-matter burial occurred on land in peat swamps, although it is likely that other reduced reservoirs such as oligotrophic or marginal marine basins, and methane clathrates, also had a role to play (e.g., Thompson and Schmitz, 1997; Beerling, 2000; Kurtz et al., 2003, Kalkreuth, 2004; Hilting et al., 2008). When the long-term warming trend was initiated ~57.7 Ma, $\delta^{13}C$ values also began a long-term decline, likely reflecting less favourable conditions for the sequestration of organic matter either on land or in the oceans (Fig. 2).

Although the long-term trends in the new benthic stable-isotope record largely replicate the gross trends known from the composite stacked records (e.g. Zachos et al., 2008), several new features can be discerned that are previously undocumented. For example, the short ~500 kyr cooling reversal in the Eocene observed in the new benthic $\delta^{18}O$ record (~54.5–55.0 Ma), interrupts the long-term warming trend and has not previously been resolved (Figs. 2, S2). The cause of this cooling is enigmatic but could have been caused by a brief, as yet unidentified, cessation of volcanogenic CO_2 production associated with the NAIP. Intriguingly, the main ash phase associated with the second phase of NAIP activity

occurred ~800 to 1100 kyr after the onset of the PETM (~54.7 –54.4 Ma), which coincides closely with the initiation of a sharp negative trend in benthic $\delta^{13}C$ values and the termination of the cooling interval, suggesting a possible volcanogenic source for both the influx of isotopically light carbon and the subsequent warming (Fig. 2; Westerhold et al., 2009; Saunders et al. 1997).

The covariance of the Site 1262 and 1209 benthic oxygen-isotope records on orbital time scales (Fig. 7) demonstrates that changes in temperature are global in scale, consistent with orbital forcing and a dominant high-latitude source of bottom waters. Minor apparent offsets (on the order of ~100 kyr) between some of the orbitally-paced oscillations in $\delta^{18}O$ and $\delta^{13}C$ between sites, may be a factor of either fine-scale age model discrepancies between the two sites or the lower sedimentation rate at Site 1209 over certain intervals, i.e., 55.5–56.5 Ma. The consistent ~0.2% offset in $\delta^{13}C$ benthic values between the Site 1262 and Site 1209 records suggests the presence of older deep / deep intermediate water in the Pacific basin compared to the South Atlantic (Fig. 7). This suggests a dominant Southern Ocean source for deep-water and longer residence time in the larger basin, similar to modern global circulation patterns, and is consistent with existing inferences regarding Paleogene ocean circulation from both low-resolution carbon-isotope compilations (e.g., Corfield 1996; Corfield and Cartlidge 1992; Cramer et al., 2009) and εNd studies (e.g., Thomas et al., 2003).

4.2. Inferred trends in lysocline depth from %CF and Fe records

The Site 1262 % CF record can be used to approximate relative changes in regional lysocline depth (e.g., Kelly et al., 2005), as in pelagic settings the %CF is largely controlled by the preservation and dissolution of planktonic foraminifera, which is strongly coupled to the depth of the regional lysocline (e.g., Broecker and Clark, 1999). Other measures such as benthic abundance and fragmentation index may provide complimentary information (e.g,,

376 Hancock and Dickens, 2005; Petrizzo et al., 2008). The depth of the lysocline is controlled
377 by a number of physiochemical conditions within the deep-ocean and uppermost part of the
378 sediment column, including temperature and the concentration of bottom water CO_3^{2-}. On
379 the time scale of higher frequency orbital cycles (<100 kyr), shifts in the flux of CO_2
380 between the ocean/atmosphere and sediment reservoirs can drive fluctuations of the CCD on
381 a global scale. On longer time scales, additional factors influence the lysocline and CCD,
382 particularly carbon emission and weathering fluxes (Ridgwell & Zeebe, 2005; Pälike et al.,
383 2012). Previous studies have revealed a dynamic and variable CCD history for the
384 Paleocene-Eocene, with significant shifts in regional carbonate preservation at depth (e.g.,
385 Zachos et al. 2004; Hancock and Dickens, 2005). These broad-scale trends in lysocline
386 depth are replicated in the %CF record at Site 1262 (Fig. 2).
387 Locally, the lysocline can shift with changes in circulation patterns, however, the
388 long-term trends in %CF values from both sites 1262 and 1209, which are plotted on the
389 same timescale, are strongly coherent through most of the record, suggesting that the
390 lysocline trends are likely global rather than regional (Fig. 7; Westerhold et al., 2011).
391 Periods of low %CF during the Late Paleocene (~58–59.5 Ma) correspond to periods of low
392 overall sedimentation rate at both Sites 1262 and 1209 (Fig. 2), which along with the low
393 $\%CaCO_3$ content suggests a relatively shallow lysocline with respect to the paleodepth of
394 the sites (Site 1262 ~3600 m; Site 1209 ~ 1500 m) (Zachos et al., 2004; Westerhold et al.,
395 2007; 2011). This shallowing of the lysocline occurs synchronously with the termination of
396 the cooling trend and the initiation of a steep positive trend in $\delta^{13}C$, suggesting a coupling
397 between long-term organic matter burial and the carbonate chemistry of the oceans.
398 The increase in sedimentation rate at ~57.7–58 Ma is matched by a concurrent
399 increase in %CF and $\%CaCO_3$, which persists into the Early Eocene, suggesting a deepening
400 of the CCD at this time in both the Pacific and the Atlantic (Fig. 2; Zachos et al., 2004;

401 Westerhold et al., 2011; Hancock and Dickens, 2005), and likely also the Indian Ocean
402 (Hancock et al., 2006). The apparent covariance between trends in CCD depth across
403 multiple ocean basins precludes regional mechanisms such as a switch in deep-ocean
404 ventilation, as that would be expected to drive opposite trends in different ocean basins (e.g.,
405 Pälike et al., 2012). Instead, with higher global temperature and humidity, the overall
406 deepening trend from the Late Paleocene to the Early Eocene could have been driven by
407 increased chemical weathering rates and thus the supply of solutes to the ocean, thereby
408 suppressing the CCD (e.g. Hilting et al., 2008), although changes in sea level and the burial
409 of neritic carbonates could also have a role to play.
410
411 **4.3. The Early Late Paleocene Event**
412 The Early Late Paleocene Event (ELPE), synonymous with the Mid Paleocene Biotic
413 Event (MPBE; 58.9 Ma), is a horizon of intense dissolution and faunal turnover, previously
414 recorded from sites on Shatsky Rise in the North Pacific, on Walvis ridge in the South
415 Atlantic, and at the Zumaia section in the western Pyrenees (Röhl et al., 2004; Petrizzo,
416 2005; Bralower et al., 2006; Bernaola et al., 2007). Existing records suggest a concurrent
417 shift in $\delta^{13}C$ values during this extremely severe dissolution event, however, poor carbonate
418 preservation at Site 1209 meant it was impossible to determine whether or not the ELPE was
419 a global hyperthermal-like event (Westerhold et al., 2011). The Site 1262 bulk and benthic
420 stable-isotope record clearly shows that the ELPE event also occurred in the Atlantic,
421 consistent with previous observations based on natural gamma-ray peaks at Site 1051 or Fe
422 intensity and $\%CaCO_3$ at ODP Leg 208 sites (e.g., Norris et al., 2001; Westerhold et al.,
423 2008). The event here is marked by the characteristically low sedimentation rates, strong
424 dissolution of carbonate, a prominent spike in Fe intensity, and $\delta^{13}C$ values which shift first
425 to more positive then to more negative values in both the benthic and bulk records (Fig. 2,

S2b). Interestingly, this event is also characterized by rapid negative excursions in $\delta^{18}O$ values, suggesting rapid warming of up to ~4ºC above background Late Paleocene temperatures of ~8ºC, making it one of the larger events of the Paleogene (Fig. S2b). The apparent oscillating nature of the $\delta^{18}O$ record during this interval, also visible in the somewhat noisy nature of the benthic $\delta^{13}C$ data, may be due to increased bioturbation and therefore reworking of foraminifera disrupting the primary stratigraphy across this event (Fig. S4). The presence of this perturbation in the Atlantic, Pacific and Northern Tethyan Ocean suggests the ELPE was a global phenomenon, likely involving a large-scale release of reduced carbon sufficient to cause significant shoaling in the already relatively shallow CCD, and causing sufficient disturbance to global climate to trigger a biotic turnover. However, the corresponding response in the carbon-isotope record was relatively minor (<0.5‰ change in benthic $\delta^{13}C$), perhaps suggesting a different mode and mechanism compared to the later and much larger hyperthermals such as the PETM. Interestingly, the ELPE marks the end of the long-term mid Paleocene cooling phase suggesting a major change in climate boundary conditions and/or the crossing of a climatic threshold into a long-term warming regime (Fig. 2).

4.4. The peak-PCIM event and onset of long-term warming

A large positive step in $\delta^{13}C$ values at ~57.7 Ma, near the middle of chron C25r and the peak of the PCIM, concurrent with a prominent negative step in $\delta^{18}O$ values, was first recognized in the high-resolution benthic record from Site 1209; however, it was unclear whether this represented a local feature related to a change in bottom water source in the North Pacific or a global signal affecting more than one ocean basin (Westerhold et al., 2011). The presence of this event in the new benthic stable-isotope records from Site 1262 in the South Atlantic clearly shows the event is global (Figs. 7; S2a). The very sharp

positive step in $\delta^{13}C$ values of 1 ‰ can be explained by a sudden shift in the proportion of carbon removed from the system through either carbonate or organic matter burial. Changes in organic burial fluxes, however, are normally associated with the relatively slow expansion (~kyr scale) of sedimentary reservoirs such as permafrost, marine organic matter, peats, or similar, which is difficult to envisage occurring sufficiently rapidly. The concurrent warming step, demonstrated by a decrease in $\delta^{18}O$ of ~0.5‰, may be related to CO_2 release from the onset of NAIP phase 2 (Figs. 7; S2a; Westerhold et al., 2011). The coeval warming and positive step in $\delta^{13}C$ values is reminiscent of the early stages of Oceanic Anoxic Events (OAEs), where warming climate led to an expansion of oxygen minimum zones or sluggish circulation and greater organic carbon burial, thus triggering a positive $\delta^{13}C$ excursion in the oceans (Kump and Arthur, 1999). It is possible that the southwest Pacific was the site of this putative excess carbon burial (Hollis et al., 2014), however, further investigation is required to reconcile the nature of carbon cycle and climate coupling during this event.

4.5. Orbital pacing of Paleogene climate and carbon-cycling

Previous studies have shown that eccentricity and precession are dominant pacemakers of Late Cretaceous–Paleogene climate and carbon cycling, as expressed by cyclic changes in lithology and stable-isotope records in marine sedimentary sequences (Herbert and Dhondt, 1990; Herbert, 1997; Pälike et al., 2006a, b; Röhl et al., 2007; Dinarès-Turell et al., 2007; Westerhold and Röhl, 2009; Voigt et al., 2012, Westerhold et al., 2007; 2008; Woodard et al., 2011). However, the apparent power at these frequencies, particularly in eccentricity, was difficult to reconcile within the context of standard orbital-climate theory. In the Site 1262 records, the strong covariance at the eccentricity frequencies between benthic $\delta^{13}C$, benthic $\delta^{18}O$ and %CF, provides insight as to the origin of the perturbations. At both the long and short eccentricity bands, negative excursions in benthic

476 $\delta^{13}C$ are matched by concurrent negative excursions in benthic $\delta^{18}O$ and %CF values
477 suggesting strong coupling of climate and the carbon cycle (Fig. 2). At both long and short
478 eccentricity maxima, increases in bottom water temperature led changes in the carbon-cycle
479 (Fig. 5), suggesting that warming climates triggered the release of light carbon from reduced
480 reservoirs, likely further enhancing warming as a positive feedback (i.e., non-linear
481 response). The accompanying reduction in %CF suggest these injections of carbon led to
482 shoaling of the CCD; however, the phasing relationship between %CF and $\delta^{13}C$ (Figs. 6, S7)
483 suggests that carbonate dissolution occurred prior to the release of the reduced carbon,
484 although this may be an artifact of post-depositional sediment burn-down during the
485 negative CIEs (e.g., Zachos et al., 2005; Panchuk et al., 2008).
486 The reservoir of ^{13}C depleted carbon responsible for fueling these orbitally-paced
487 CIEs is currently unknown, though there are several options. Based on sedimentary records
488 of thick coal deposits and marine isotopic records, it is assumed that large volumes of
489 organic matter were periodically stored on the land in the form of peat during the latest
490 Paleocene, likely due to the relatively cool greenhouse conditions which prevailed at the
491 time (e.g., Shackleton, 1986; Beerling, 2000; Kurtz et al., 2003, Hilting et al., 2008; Shearer
492 et al., 1995; Ziegler et al., 2003; Kalkreuth, 2004). Similarly, large masses of reduced carbon
493 might have accumulated in permafrost on Antarctica and in the circum-Arctic during this
494 time, due to the absence of a large ice-cap and the exposure of carbon-rich tundra and forest
495 ecosystems to seasonally freezing conditions (e.g., DeConto et al., 2012). Another
496 potentially large sedimentary source of light carbon is methane hydrate, which is likely to
497 have existed in the warm, relatively organic-rich Paleogene shelf regions (e.g., Dickens,
498 2011). In theory, all three of the aforementioned reduced carbon reservoirs should have been
499 sensitive to variations in orbital forcing and climate, and possibly responding in kind.

Eccentricity largely affects climate through the modulation of precession, in that precession has its greatest influence when eccentricity is at its maximum, which can clearly be seen in filter outputs of the new Site 1262 record, where the amplitude of precession co-varies with the amplitude of both long and short eccentricity (Fig. 3; e.g., Herbert, 1997). In theory, methane hydrate deposits on the continental shelves and slopes would be very sensitive to the small increase in average temperature associated with high eccentricity and precession (Lunt et al. 2011). Any such release of biogenic methane would be characterized by a sharp negative excursion in carbon isotopes, accompanied by enhanced warming through climate-carbon-cycle feedback mechanisms and potentially further destabilization of methane deposits (e.g., Dickens, 2011). However, the extent of methane hydrate reserves in a much warmer world than the present is contentious, and even modern inventories are the subject of continuing debate (e.g., Kvenvolden & Lorenson, 2001; Buffett & Archer, 2004; Gu et al., 2011).

Both low-latitude peat and high-latitude permafrost could potentially be responsive to small changes in climate associated with eccentricity-modulated precessional changes in seasonal insolation. Low-latitude peat extent in the early Paleogene is likely to have been sensitive to changes in precipitation patterns, in the same way that African lake levels are strongly correlated to precession-driven changes in precipitation in the Pleistocene, with eccentricity as an additional modulator (e.g., Trauth et al., 2007). High eccentricity (high precession) would have driven more seasonally uneven rainfall on the continents creating "monsoon like" conditions (e.g., Short et al., 1991; Crowley et al., 1992; Rutherford and D'Hondt, 2000) less conducive to the storage of organic matter, and leading to periodic variations in the flux of carbon to and from the soil reservoirs (Zachos et al., 2010).

Permafrost may also be sensitive to changing insolation; however, it is more likely to be sensitive to direct changes in temperature associated with both longer and more intense

525 insolation during summer months during precessional maxima, as warming would cause a
526 loss in the area of land able to sustain sub-freezing conditions throughout the year (e.g.,
527 Schuur et al., 2008; DeConto et al., 2012). A strong 405 kyr beat in Antarctic ice coverage,
528 in step with changes in the carbon-cycle, has recently been modelled for the last 5 Ma,
529 suggesting that the polar regions are very sensitive to long eccentricity forcing (de Boer et
530 al., 2014). It may be that even during periods of relatively low ice volume, such as the
531 Paleogene, this sensitivity to eccentricity remained, expressed in terms of the response in the
532 extent of permafrost regions. Indeed, the lack of a coherent obliquity signal in any of the
533 Site 1262 isotopic or %CF records (Figs. 4, 6), suggests that polar ice volumes were
534 minimal during the Early Paleogene, as glaciated high-latitudes are known to be particularly
535 sensitive to obliquity forcing in other periods of time such as the Neogene (e.g., Raymo and
536 Nisancioglu, 2003; Huybers & Wunsch, 2005; Naish et al., 2009). This stands in contrast to
537 other lower-resolution Late Paleocene–Early Eocene marine stable-isotope records, which
538 have suggested an obliquity beat is one of the dominant components of the coupled climate-
539 carbon-cycle at this time (e.g., DeConto et al., 2012).

540 Interestingly, the onset of the long-term negative trend in $\delta^{13}C$ values at ~57.7 Ma
541 also marks a transition toward more pronounced eccentricity-paced excursions in climate
542 ($\delta^{18}O$) and the carbon cycle ($\delta^{13}C$) that characterize the latest Paleocene (Fig. 2), suggesting
543 a generally higher sensitivity to orbital forcing during this time. In theory, a sudden rise in
544 CO_2 emissions along with warming would enhance processes sequestering carbon, from
545 rock weathering to productivity to carbon burial, as manifested by the jump in carbonate
546 accumulation at 57.7 Ma. The dynamics of climate-carbon cycle feedbacks (i.e., non-linear)
547 might have shifted as well so as to enhance sensitivity to orbital forcing, leading to larger
548 amplitude cycles. Alternatively, the large stocks of reduced sedimentary carbon (in either
549 methane, permafrost, or peat), built up during the PCIM, were now primed for

550 destabilisation and release during the transient warmer intervals associated with eccentricity
551 maxima. As the long-term warming trend progressed from the late Paleocene through the
552 early Eocene, the volumes of reduced carbon would have been reduced, leading to
553 progressively smaller 405-kyr cycle paced perturbations in the Early Eocene (e.g., DeConto
554 et al., 2012; Fig. 2).

555 The changing phase relationship through time between $\delta^{18}O$ and $\delta^{13}C$ at the 405-kyr
556 band, could potentially offer clues as to the underlying mechanisms, although a change in
557 phasing is not unexpected as other boundary conditions (e.g. pCO_2, sea level, and gateways)
558 were also shifting over this time. Close coupling of climate and the carbon cycle is inferred
559 for the latest Paleocene (lag of only ~4 (±5) kyr between $\delta^{18}O$ and $\delta^{13}C$ at the 405-kyr band)
560 when reduced carbon reservoirs (e.g., methane, permafrost) were apparently large and the
561 system was very sensitive to eccentricity forcing (Fig. S5), whereas the coupling became
562 less close in the very warm Early Eocene interval (~21 (±2) kyr lag between $\delta^{18}O$ and $\delta^{13}C$),
563 likely due to smaller and less sensitive stocks of reduced carbon, e.g., where higher
564 temperatures reduced the available area of possible storage of methane clathrates on the
565 continental shelves (e.g., Dickens et al., 1995; Dickens, 2011; Komar et al., 2013).

566 As previously noted (Zachos et al., 2010), although the initiation of the PETM may
567 have been in-phase with the 100-kyr cycle, it does not appear to be in phase with the 405-
568 kyr cycle. Additionally, in spite of the clear long-term warming trend in $\delta^{18}O$ from the latest
569 Paleocene through to the earliest Eocene, there is little difference in the minimum $\delta^{18}O$
570 values reached during the ~1.5 myrs prior to the PETM, as the 100 kyr-paced events such as
571 the D2 and C2 all reach values of ~0.3 ‰ (Fig. S5). This, in combination with the very high
572 amplitude and the extended recovery time of the event, suggests that the PETM required an
573 extra "push" to achieve such extreme warming and carbon-cycle disruption. This is likely to
574 have involved the catastrophic addition of extra carbon from sedimentary sources such as

methane clathrates, permafrost, or thermogenic methane, not necessarily triggered by changes in orbitally-paced insolation, but purely as a positive feedback.

5. Summary

The 7.7 myr long, orbitally-tuned benthic stable-isotope record from the South Atlantic ODP Site 1262 is the longest stratigraphically complete record spanning the Late Paleocene and Early Eocene. The long-term trends in the carbon-cycle closely follow those known from the existing bulk carbon-isotope record from this site and the stacked global benthic record, however, the new benthic oxygen-isotope record reveals interesting previously unknown features, such as the abrupt warming step at the peak of the PCIM at 57.7 Ma, and the brief cooling reversal in the earliest Eocene ~54.7 Ma.

The high-resolution nature of the benthic record allows the power and phasing of high-frequency orbitally-paced variations to be resolved, which are clearly dominated by precession and eccentricity. Changes in the distribution of heat and precipitation associated with eccentricity cycles (and modulation of precession) likely influenced the flux into and out of sedimentary reduced carbon reservoirs such as permafrost, peat, or methane hydrates. The increasing lag between benthic $\delta^{18}O$ and $\delta^{13}C$ records at the 405-kyr band suggests a progressively weakening of the connection between climate and the carbon-cycle from the Late Paleocene into the Early Eocene. The lack of power in the obliquity band throughout the record strongly suggests a low polar ice-volume during the Early Paleogene, in-line with other paleontological and geochemical proxies for global warmth at this time.

Acknowledgements

Thanks to Alexis Kersey for picking foraminifera and assisting with sample processing (at UCSC), and to Walker Weir, Alejandro Aguilar, and Phillip Staudigel for lab

assistance, and to Dyke Andreasen and Chih-Ting Hsieh for stable-isotope support (UCSC). Thanks to Barbara Donner (MARUM) for coordinating foraminifera picking, and to Monika Segl and her team (MARUM) for stable-isotope analyses. We thank Roy Wilkens (Hawaii) for core images analysis. Sediment samples were supplied by the Ocean Drilling Program. Funding for this project was provided by NSF grant (grant number EAR-0628719) to J.Z and DFG grants (RO 1113/2 through RO 1113/4) to U.R/ T.W.

Appendix A. Supplementary data

Supplementary materials related to this article can be found online at *doi: XXXXXX [Address to be confirmed upon publication]*.

7. References

Agnini, C., Backman, J., Brinkhuis, H., Fornaciari, E., Giusberti, L., Luciani, V., Rio, D., Sluijs, A., 2009. An early Eocene carbon cycle perturbation at similar to 52.5 Ma in the Southern Alps: chronology and biotic response. Paleoceanography 24.

Arthur, M. A., 1980. The carbon cycle: Controls on the atmospheric CO2 and climate in the geological past, in Climate in Earth History, pp. 55–67, Natl. Acad. Press, Washington, D. C.

Beerling, D.J., 2000. Increased terrestrial carbon storage across the Palaeocene–Eocene boundary. Palaeogeogr. Palaeoclimatol. Palaeoecol. 161, 395–405.

Bemis, B.E., Spero, H.J., Bijma, J., Lea, D.W. 1998. Reevaluation of the oxygen isotopic composition of planktic foraminifera: Experimental results and revised paleotemperature equations. Paleoceanography, 13(2), 150–160.

Bernaola, G., Baceta, J. I. Orue-Etxebarria, X. Alegret, L. Martin Rubio, M. Arostegui, J., Dinarès-Turell, J., 2007. Evidence of an abrupt environmental disruption during the mid-Paleocene biotic event (Zumaia section, western Pyrenees), Geol. Soc. Am. Bull., 119, 785–795, doi:10.1130/B26132.1.

Bijl, P.K., Schouten, S., Sluijs, A., Reichart, G-J., Zachos, J.C., Brinkhuis, H., 2009. Early Palaeogene temperature evolution of the southwest Pacific Ocean. Nature 461, 776–779. doi:10.1038/nature08399.

Bralower, T. J., Premoli Silva, I., Malone. M. J., 2006. Leg 198 synthesis: A remarkable 120-m.y. record of climate and oceanography from Shatsky Rise, northwest Pacific Ocean, Proc. Ocean Drill. Program. Sci. Results, 198, 47 pp., doi:10.2973/odp.proc.sr.198.101.2006.

Broecker, W.S., Clark, E., 1999. $CaCO_3$ size distribution: a paleocarbonate ion proxy? Paleoceanography 14 (5), 596–604.

Buffett, B., Archer, D. 2004. Global inventory of methane clathrate: Sensitivity to changes in the deep ocean. Earth Planet. Sci. Lett. 227, 185–199.

650 Coccioni, R., Frontalini, F., Bancalà, G., Fornaciari, E, Jovane, L., Sprovieri, M., 2010.
651 The Dan-C2 hyperthermal event at Gubbio (Italy): Global implications, environmental
652 effects, and cause(s), Earth Planet. Sci. Lett., 297, 298–305.
653 doi:10.1016/j.epsl.2010.06.031.
654
655 Corfield, R.M., Norris, R.D., 1996. Deep water circulation in the Paleogene Ocean. In:
656 Knox, R.W., Corfield, R.M., Dunay, R.E. (Eds.), Correlation of the Early Paleogene in
657 Northwest Europe. : Geological Society Special Publication. Geological Society,
658 London, pp. 443–456.
659
660 Corfield, R. M., Cartlidge, J.E., 1992. Oceanographic and climatic implications of the
661 Palaeocene carbon isotope maximum, Terra Nova, 4(4), 443–455, doi:10.1111/j.1365-
662 3121.1992.tb00579.x.
663
664 Cramer, B.S., Wright, J.D., Kent, D.V., Aubry, M.P., 2003. Orbital climate forcing of
665 $\delta^{13}C$ excursions in the late Paleocene-early Eocene (chrons C24n-C25n).
666 Paleoceanography 18, 1097.
667
668 Cramer, B. S., Toggweiler, J. R., Wright, J. D., Katz, M. E., Miller, K. G., 2009. Ocean
669 overturning since the Late Cretaceous: Inferences from a new benthic foraminiferal
670 isotope compilation. Paleoceanography 24, PA4216. doi:10.1029/2008PA001683.
671
672 Crowley, T.J., Kim, K.Y., Mengel, J.G., Short, D.A., 1992. Modeling 100,000-year
673 climate fluctuations in Pre-Pleistocene time-series. Science 255 (5045), 705–707.
674

675 DeConto, R.M., Galeotti, S., Pagani, M., Tracy, D., Schaefer, K., Zhang, T., Pollard, D.,
676 Beerling, D.J., 2012. Past extreme warming events linked to massive carbon release
677 from thawing permafrost. Nature 484, 87–92. doi:10.1038/nature10929.
678
679 Dickens, G.R., O'Neill, J.R., Rea, D.K., Owen, R.M., 1995. Dissociation of oceanic
680 methane hydrate as a cause of the carbon isotope excursion at the end of the Paleocene.
681 Paleoceanography 10, 965–971.
682
683 Dickens, G.R., Castillo, M.M., Walker, J.C.G., 1997. A blast of gas in the latest
684 Paleocene: simulating first-order effects of massive dissociation of oceanic methane
685 hydrate. Geology 25, 259–262.
686
687 Dickens, G.R., 2011. Down the Rabbit Hole: toward appropriate discussion of methane
688 release from gas hydrate systems during the Paleocene-Eocene thermal maximum and
689 other past hyperthermal events. Clim. Past. 7, 831–846.
690
691 Dinarès-Turell, J., Baceta, J. I., Bernaola, G., Orue-Etxebarria, X., Pujalte, V., 2007.
692 Closing the Mid-Palaeocene gap: Toward a complete astronomically tuned Palaeocene
693 Epoch and Selandian and Thanetian GSSPs at Zumaia (Basque Basin, W Pyrenees).
694 Earth Planet Sci. Lett. 262, 450–467.
695
696 Friedrich, O., Norris, R.D., Erbacher, J., 2012. Evolution of middle to Late Cretaceous
697 oceans—A 55 m.y. record of Earth's temperature and carbon cycle. Geology 40, 107–
698 110.
699

700 Galeotti, S., Krishnan, S., Pagani, M., Lanci, L., Gaudio, A., Zachos, J.C., Monechi, S.,
701 Morelli, G., Lourens, L., 2010. Orbital chronology of Early Eocene hyperthermals from
702 the Contessa Road section, central Italy. Earth. Planet. Sci. Lett. 290, 192–200.
703
704 Gu, G., Dickens, G.R., Bhatnagar, G., Colwell, F.S., Hirasaki, G.J., Chapman, W.G.,
705 2011. Abundant Early Palaeogene marine gas hydrates despite warm deep-ocean
706 temperatures. Nat. Geosci. 4, 848–851. doi: 10.1038/NGEO1301.
707
708 Hancock, H.J.L., Dickens, G.R., Thomas, E., Blake, K.L., 2006. Reappraisal of early
709 Paleogene CCD curves: foraminiferal assemblages and stable carbon isotopes across the
710 carbonate facies of Perth Abyssal Plain. Int. J. Earth. Sci. (Geol Rundsch). doi:
711 10.1007/s00531-006-0144-0.
712
713 Hancock, H.J.L., Dickens, G.R., 2005. Carbonate dissolution episodes in Paleocene and
714 Eocene sediment, Shatsky Rise, west-central Pacific. In: Bralower TJ, Premoli Silva I,
715 Malone MJ (eds) Proceedings of ODP, science results, 198.
716
717 Herbert, T.D., Dhondt, S.L., 1990. Precessional climate cyclicity in late cretaceous early
718 tertiary marine sediments — a high resolution chronometer of cretaceous tertiary
719 boundary events. Earth Planet. Sci. Lett. 99, 263–275.
720
721 Herbert, T.D., 1997. A long marine history of carbon cycle modulation by orbital–
722 climatic changes. Proc. Natl. Acad. Sci. USA 94 (16), 8362–8369.
723

724 Higgins, J.A., Schrag, D.P., 2006. Beyond methane: towards a theory for the Paleocene–
725 Eocene Thermal Maximum. Earth Planet. Sci. Lett. 245, 523–537.
726
727 Hilgen, F.J., Kuiper, K.F., Lourens, L.J., 2010. Evaluation of the astronomical time scale
728 for the Paleocene and earliest Eocene. Earth Planet. Sci. Lett. 300, 139–151.
729
730 Hilting, A.K., Kump, L.R., Bralower, T.J., 2008. Variations in the oceanic vertical
731 carbon isotope gradient and their implications for the Paleocene-Eocene biological
732 pump, Paleoceanography 23, PA3222. doi:10.1029/2007PA001458.
733
734 Hollis, C.J., Taylor, K.W.R., Handley, L., Pancost, R.D., Huber, M., Creech, J.B., Hines,
735 B.R., Crouch, E.M., Morgans, H.E.G., Crampton, J.S. Gibbs, S., Pearson, P.N., Zachos,
736 J.C., 2012. Early Paleogene temperature history of the Southwest Pacific Ocean:
737 Reconciling proxies and models. Earth Planet Sci. Lett. 349–350, 53–66.
738
739 Hollis, C.J., Tayler, M.J.S., Andrew, B., Taylor, K.W., Lurcock, P., Bijl, P.K.,
740 Kulhanek, D. K., Crouch, E.M., Nelson, C.S., Pancost, R.D., Huber, M., Wilson, G.S.,
741 Ventura, G.T., Crampton, J.S., Schiøler, P., Phillips, A., 2014. Organic-rich
742 sedimentation in the South Pacific Ocean associated with Late Paleocene climatic
743 cooling. Earth Science Reviews 134, 81–97.
744
745 Huybers, P., Wunsch, C., 2005. Obliquity pacing of the late Pleistocene glacial
746 terminations. Nature 434, 491–494.
747
748 Kalkreuth, W. D., 2004. Coal facies studies in Canada. International Journal of Coal

749 Geology 58, 23–30.
750
751 Katz, M.E., Katz, D.R., Wright, J.D., Miller, K.G., Pak, D.K., Shackleton, N.J., Thomas,
752 E., 2003. Early Cenozoic benthic foraminiferal isotopes: Species reliability and
753 interspecies correction factors. Paleoceanography 18, 1024.
754
755 Kelly, C.D., Zachos, J.C., Bralower, T.J., Schellenberg, S.A., 2005. Enhanced terrestrial
756 weathering/runoff and surface ocean carbonate production during the recovery stages of
757 the Paleocene-Eocene thermal maximum. Paleoceanography 20, PA4023.
758
759 Kennett, J.P., Stott, L.D.S., 1991. Abrupt deep-sea warming, palaeoceanographic
760 changes and benthic extinctions at the end of the Palaeocene. Nature 353, 225–229.
761
762 Komar, N., Zeebe, R.E., Dickens, G.R., 2013. Understanding long-term carbon-cycle
763 trends: the Late Paleocene through the Early Eocene. Paleoceanography 28, 650–662.
764
765 Kurtz, A., Kump, L.R., Arthur, M.A., Zachos, J.C., Paytan, A., 2003. Early Cenozoic
766 decoupling of the global carbon and sulphur cycles. Paleoceanography 18, 1090.
767
768 Kent, D. V., B. S. Cramer, L. Lanci, D. Wang, J. D.Wright, Van der Voo, R., 2003. A
769 case for a comet impact trigger for the Paleocene/ Eocene thermal maximum and carbon
770 isotope excursion, Earth Planet. Sci. Lett. 211, 13–26.
771
772 Kump, L. R., Arthur, M. A., 1999. Interpreting carbon-isotope excursions: Carbonates
773 and organic matter, Chem. Geol., 161(1–3), 181–198, doi:10.1016/S0009-

774 2541(99)00086-8.
775
776 Kvenvolden, K. A., Lorenson, T.D., 2001. The global occurrence of natural gas hydrate.
777 Geophysical Monograph Series 124, 3–18.
778
779 Laskar, J., Robutel, P., Joutel, F., Gastineau, M., Correia, A.C.M., Levrard, B., 2004. A
780 long-term numerical solution for the insolation quantities of the Earth. Astronomy &
781 Astrophysics 428, 261–285.
782
783 Lourens, L.J., Sluijs, A., Kroon, D., Zachos, J.C., Thomas, E., Röhl, U., Bowles, J.,
784 Raffi, I., 2005. Astronomical pacing of late Palaeocene to early Eocene global warming
785 events. Nature 435, 1083–1087.
786
787 Lunt, D. L., Valdes, P. J., Dunkley Jones, T., Ridgwell, A., Haywood, A. M., Schmidt,
788 D. N., Marsh, R., Maslin, M., 2010. CO_2-driven ocean circulation changes as an
789 amplifier of Paleocene-Eocene thermal maximum hydrate destabilization. Geology 38,
790 875–878.
791
792 Lunt, D.J., Ridgwell, A., Sluijs, A., Zachos, J.C., Hunter, S., Haywood, A., 2011. A
793 model for orbital pacing of methane hydrate destabilization during the Palaeogene.
794 Nature Geoscience 4, 775–778. doi:10.1038/ngeo1266.
795
796 Mann, M. E., Lees, J.M., 1996. Robust estimation of background noise and signal
797 detection in climatic time series, Clim. Change, 33(3), 409–445.
798 doi:10.1007/BF00142586.

McInerney, F.A., Wing, S. L., 2011. The Paleocene-Eocene Thermal Maximum: A Perturbation of Carbon Cycle, Climate, and Biosphere with Implications for the Future. Annu. Rev. Earth Planet. Sci. Lett. 39, 489–516.

McCarren, H., Thomas, E., Hasegawa, T., Röhl, U., Zachos, J.C., 2008. Depth dependency of the Paleocene-Eocene carbon isotope excursion: Paired benthic and terrestrial biomarker records (Ocean Drilling Program Leg 208, Walvis Ridge), Geochem. Geophys. Geosyst. 9, Q10008. doi:10.1029/2008GC002116.

Naish, T., R. et al., 2009. Obliquity-paced Pliocene West Antarctic ice sheet oscillations. Nature 458, 322–329, doi:10.1038/nature07867.

Nicolo, M., Dickens, G.R., Hollis, C.J., Zachos, J.C., 2007. Multiple early Eocene hyperthermals: their sedimentary expression on the New Zealand continental margin and in the deep sea. Geology 35, 699–702.

Norris, R.D., Kroon, D., Klaus, A., eds., 2001. Western North Atlantic Palaeogene and Cretaceous Palaeoceanography: Geological Society [London] Special Publication, 183, 163-183.

Pagani, M., Zachos, J.C. Freeman, K.H., Tipple, B., Bohaty, S. 2005. Marked Decline in Atmospheric Carbon Dioxide Concentrations During the Paleogene. Science 309, 600–603.

824 Paillard, D., Labeyrie, L., Yiou, P., 1996. Macintosh program performs time-series
825 analysis. EOS Trans. AGU 77, 379.
826
827 Pälike, H., Norris, R.D., Herrle, J.O., Wilson, P.A., Coxall, H.K., Lear, C.H.,
828 Shackleton, N.J., Tripati, A.K., Wade, B.S., 2006a. The heartbeat of the Oligocene
829 climate system. Science 314, 1894–1898.
830
831 Pälike, H., J. Frazier, Zachos, J.C., 2006b, Extended orbitally forced palaeoclimatic
832 records from the equatorial Atlantic Ceara Rise. Quaternary Sci. Rev. 25, 3138–3149.
833 doi: 10.1016/j.quascirev.2006.02.011.
834
835 Pälike, et al., 2012. A Cenozoic record of the equatorial Pacific carbonate compensation
836 depth. Nature 488, 609–615.
837
838 Panchuk, K., Ridgwell, A. Kump, L.R., 2008. Sedimentary response to Paleocene-
839 Eocene Thermal Maximum carbon release: A model-data comparison. Geology 36, 315–
840 318.
841
842 Petrizzo, M.R., 2005. An early late Paleocene event on Shatsky Rise, northwest Pacific
843 Ocean (ODP Leg 198): evidence from planktonic foraminiferal assemblages. In
844 Bralower, T.J., Premoli Silva, I., and Malone, M.J. (Eds.), Proc. ODP, Sci. Results, 198.
845
846 Petrizzo, M.R., Leoni, G., Speijer, R.P., De Bernardi, B., Felletti, F., 2008. Dissolution
847 susceptibility of some Paleogene planktonic foraminifera from ODP Site 1209 (Shatsky
848 Rise, Pacific Ocean). J. Foram. Res. 38, 357–371.

Quillévéré, F., Norris, R.D., Kroon, D., Wilson, P.A., 2008. Transient ocean warming and shifts in carbon reservoirs during the early Danian. Earth Planet. Sci. Lett., 265, 600–615. doi:10.1016/j.epsl.2007.10.040.

Rampino, M.R., 2013. Peraluminous igneous rocks as an indicator of thermogenic methane release from the North Atlantic Volcanic Province at the time of the Paleocene Eocene Thermal Maximum (PETM). Bulletin of Volcanology 75, 1–5.

Raymo, M.E., Nisancioglu, K., 2003. The 41 kyr world: Milankovitch's other unsolved mystery. Paleoceanography 18, doi:10.1029/2002PA000791.

Ridgwell, A., Zeebe, R., 2005. The role of the global carbonate cycle in the regulation and evolution of the Earth system. Earth Planet. Sci. Lett. 234, 299–315.

Röhl, U., Westerhold, T., Bralower, T.J., Petrizzo, M.-R., and Zachos, J.C., 2004. An early late Paleocene global dissolution event and new constraints for an astronomically-tuned early Paleogene time scale, paper presented at 8th International Conference on Paleoceanography, Environ. et Paleonenviron. Oceanique, Biarritz, France, 5–10 Sept.

Röhl, U., Westerhold, T., Bralower, T.J., Zachos, J.C., 2007. On the duration of the Paleocene–Eocene thermal maximum (PETM). Geochem. Geophys. Geosyst. 8, 12. doi:10.1029/2007GC001784.

873 Royer DL, Berner RA, Park J., 2007. Climate sensitivity constrained by CO2
874 concentrations over the past 420 million years. Nature 446, 530-532.
875
876 Rutherford, S., D'Hondt, S., 2000. Early onset and tropical forcing of 100,000-year
877 Pleistocene glacial cycles. Nature 408, 72–75.
878
879 Saunders, A.D., Fitton, J.G., Kerr, A.C., Norry, M.J., Kent, R.W., 1997. The North
880 Atlantic Igneous Province. In: Mahoney, J.J., Coffin, M.F. (Eds.), Large Igneous
881 Provinces: Continental, Oceanic and Planetary. Geophysical Monograph, vol. 100.
882 American Geophysical Union, Washington, DC, pp. 45–93.
883
884 Saunders, A.D., Jones, S.M., Morgan, L.A., Pierce, K.L.Widdowson, M., Xu, Y.G.
885 2007. Regional uplift associated with continental large igneous provinces: The roles of
886 mantle plumes and the lithosphere. Chemical Geology 241, 282–318.
887
888 Shackleton, N. J., Hall, M.A., Boersma, A., 1984. Oxygen and carbon isotope data from
889 Leg 74 foraminifers, Initial Rep. Deep Sea Drill. Vol 74, 599–613.
890 doi:10.2973/dsdp.proc.74.116.1984.
891
892 Shackleton, N.J., 1986. Paleogene stable isotope events. Palaeogeogr. Palaeoclimatol.
893 Palaeoecol. 57, 91–102.
894
895 Shearer, J.C., Moore, T.A., Demchuk, T.D., 1995. Delineation of the distinctive nature
896 of Tertiary coal beds. International Journal of Coal Geology 28, 71–98.
897

898 Short, D.A., Mengel, J.G., Crowley, T.J., Hyde, W.T., North, G.R., 1991. Filtering of
899 Milankovitch cycles by Earth's geography. Quatern. Res. 35 (2), 157–173.
900
901 Schrag, D.P., dePaolo, D.J., Richter, F.M., 1995. Reconstructing past sea surface
902 temperatures: correcting for diagenesis of bulk marine carbonate. Geochem.
903 Cosmochem. Acta 59, 2265–2278.
904
905 Schuur, E. A. G., Bockheim, J., Canadell, J.G., Euskirchen, E., Field, C.B., Goryachkin,
906 S.V., Hagemann, S., Kuhry, P., Lafleur, P., Lee, H., Mazhitova, G., Nelson, F.E., Rinke,
907 A., Romanovsky. V., Shiklomanov, N., Tarnocai, C., Venevsky, S., Vogel, J.G., Zimov,
908 S.A., 2008. Vulnerability of permafrost carbon to climate change: implications for the
909 global carbon cycle. Bioscience 58, 701–714.
910
911 Sinton, C. W., Duncan, R.A., 1998. 40Ar/39Ar ages of lavas from the southeast
912 Greenland margin, ODP Leg 152, and the Rockall Plateau, DSDP Leg 81, Proc. Ocean
913 Drill. Program Sci. Results, 152, 387–402. doi:10.2973/odp.proc.sr.152.234.1998.
914
915 Sluijs, A., Schouten, S., Pagani, M., Woltering, M., Brinkhuis, H., Sininnghe Damste,
916 J.S., Dickens, G.R., Huber, M., Reichart, G-J., Stein, R., Matthiessen, J., Lourens, L.J.,
917 Pedentchouk, N., Backman, J., Moran, K., and the Expedition 302 Scientists., 2006.
918 Subtropical Arctic Ocean temperatures during the Palaeocene/ Eocene thermal
919 maximum. Nature 441, 610–613.
920
921 Sluijs, A., Brinkhuis, H., Schouten, S., Bohaty, S.M., John, C.M., Zachos, J.C., Reichart,
922 G.-J., Sinninghe Damste, J.S., Crouch, E.M., Dickens, G.R., 2007. Environmental

923 precursors to rapid light carbon injection at the Palaeocene/Eocene boundary. Nature
924 450, 1218–1221. doi:10.1038/ nature06400.
925
926 Sluijs, A., Schouten, S., Donders, T.H., Schoon, P.L., Röhl, U., Reichart, G-J.,
927 Sangiorgi, F., Kim, J-H., Sinninghe Damste, J.S., Brinkhuis, H., 2009. Warm and wet
928 conditions in the Arctic region during Eocene Thermal Maximum 2. Nat. Geosci. 2,
929 777–780.
930
931 Stap, L., Sluijs, A., Thomas, E., Lourens, L., 2009. Patterns and magnitude of deep sea
932 carbonate dissolution during Eocene Thermal Maximum 2 and H2, Walvis Ridge,
933 Southeastern Atlantic Ocean. Paleoceanography 24.
934
935 Stap, S., Lourens, L.J., Thomas, E., Sluijs, A., Bohaty, S., Zachos, J.C., 2010a. High-
936 resolution deep-sea carbon and oxygen isotope records of Eocene Thermal Maximum 2
937 and H2. Geology 38, 607–610.
938
939 Stap, L., Lourens, L.J., van Dijk, A., Schouten, S., Thomas, E., 2010b. Coherent pattern
940 and timing of the carbon isotope excursion and warming during Eocene Thermal
941 Maximum 2 as recorded in planktic and benthic foraminifera. Geochem. Geophys.
942 Geosyst. 11, Q11011. doi:10.1029/2010GC003097.
943
944 Storey, M., Duncan, R.A., Swisher, C.C., 2007. Paleocene–Eocene thermal maximum
945 and the opening of the northeast Atlantic. Science 316, 587–589.
946
947 Svensen, H., Planke, S., Malthe-Sorenssen, A., Jamtveit, B., Myklebust, R., Eidem, T.R.,

948 Rey, S.S., 2004. Release of methane from a volcanic basin as a mechanism for initial
949 Eocene global warming. Nature 429, 524–527.
950
951 Thompson, E. I., Schmitz, B., 1997. Barium and the late Paleocene $\delta^{13}C$ maximum:
952 Evidence of increased marine surface productivity. Paleoceanography 12, 239–254,
953 doi:10.1029/96PA03331.
954
955 Thomas, D.J., Bralower, T.J., Jones, C.E., 2003. Neodymium isotopic reconstruction of
956 late Paleocene–early Eocene thermohaline circulation. Earth Planet Sci. Lett. 209, 309–
957 322.
958
959 Trauth, M.H., Maslin, M.A., Deino, A.L., Strecker, M.R., Bergner, A.G.N., Dühnforth,
960 M., 2007. High- and low-latitude forcing of Plio-Pleistocene East African climate and
961 human evolution. Journal of Human Evolution 53, 475–486.
962
963 Tripati, A., Elderfield, H., 2005. Deep-sea temperature and circulation changes at the
964 Paleocene–Eocene thermal maximum. Science 308, 1894–1898.
965
966 Voigt, S., Gale, A.S., Jung, C., Jenkyns, H.C., 2012. Global correlation of Upper
967 Campanian–Maastrichtian successions using carbon-isotope stratigraphy: development
968 of a new Maastrichtian Timescale. Newsletters on Stratigraphy 45/1, 25–53.
969
970 Westerhold, T., Röhl, U., Laskar, J., Raffi, I., Bowles, J., Lourens, L.J., Zachos, J.C.,
971 2007. On the duration of magnetochrons C24r and C25n and the timing of early Eocene
972 global warming events: implications from the Ocean Drilling Program Leg 208 Walvis

973 Ridge depth transect. Paleoceanography 22.
974
975 Westerhold, T., Röhl, U., Raffi, I., Fornaciari, E., Monechi, S., Reale, V., Bowles, J.,
976 Evans, H.F., 2008. Astronomical calibration of the Paleocene time. Palaeogeogr.
977 Palaeoclimatol. Palaeoecol. 257, 377–403.
978
979 Westerhold, T., Röhl, U., 2009. High resolution cyclostratigraphy of the early Eocene -
980 new insights into the origin of the Cenozoic cooling trend. Climate of the Past, 5, 309-
981 327. doi:10.5194/cp-5-309-2009.
982
983 Westerhold, T., Röhl, U., McCarren, H.K., Zachos, J.C., 2009. Latest on the absolute
984 age of the Paleocene–Eocene Thermal Maximum (PETM): New insights from exact
985 stratigraphic position of key ash layers +19 and −17. Earth Planet Sci. Lett. 287, 412–
986 419.
987
988 Westerhold, T., Röhl, U. Donner, B., McCarren, H. K., Zachos, J. C., 2011. A complete
989 high-resolution Paleocene benthic stable isotope record for the central Pacific (ODP
990 Site1209). Paleoceanography 26, PA2216. doi:10.1029/2010PA002092.
991
992 Wieczorek, R., Fantle, M.S., Kump, L.R., Ravizza, G., 2013. Geochemical evidence for
993 volcanic activity prior to and enhanced terrestrial weathering during the Paleocene
994 Eocene Thermal Maximum. Geochimica et Cosmochimica Acta 119, 391–410.
995

996 Woodard, S. C., Thomas, D. J., Hovan, S., Röhl, U., Westerhold, T. 2011. Evidence for
997 eccentricity forcing of dust accumulation during the early Paleogene greenhouse,
998 Geochem. Geophys. Geosyst. 12, Q02007. doi:10.1029/2010GC003394.
999
1000 Zachos, J. C., Pagani,M., Sloan,L., Thomas, E., Billups, K., 2001. Trends, rhythms, and
1001 aberrations in global climate 65 Ma to present. Science 292, 686–693.
1002
1003 Zachos, J. C., Shackleton, N. J., Revenaugh, J. S., Pälike, H., Flower, B. P., 2001,
1004 Climate response to orbital forcing across the Oligocene-Miocene boundary. Science
1005 292, 274–277.
1006
1007 Zachos, J. C., et al. 2004. Early Cenozoic Extreme Climates: The Walvis Ridge
1008 Transect. Proc. Ocean Drill. Program Initial Rep., vol. 208, U. S. Gov. Print. Off.,
1009 Washington, D. C. doi:10.2973/odp.proc.ir.208.2004.
1010
1011 Zachos, J. C., Röhl, U., Schellenberg, S.A., Sluijs, A., Hodell, D.A., Kelly, D.C.,
1012 Thomas, E., Nicolo, M., Raffi, I., Lourens, L.J., McCarren, H., Kroon, D., 2005. Rapid
1013 acidification of the ocean during the Paleocene-Eocene thermal maximum. Science 308,
1014 1611–1615. doi:10.1126/science.1109004.
1015
1016 Zachos, J. C., Dickens, G. R., Zeebe, R.E., 2008. An early Cenozoic perspective on
1017 greenhouse warming and carbon-cycle dynamics. Nature 451, 279–283.
1018 doi:10.1038/nature06588
1019
1020 Zachos, J. C., McCarren, H., Murphy, B., Röhl, U., Westerhold, T., 2010. Tempo and

scale of late Paleocene and early Eocene carbon isotope cycles: Implications for the origin of hyperthermals, Earth Planet. Sci. Lett. 299, 242–249. doi:10.1016/j.epsl.2010.09.004.

Zeebe, R. E., Zachos, J.C., Dickens, G.R., 2009. Carbon dioxide forcing alone insufficient to explain Palaeocene-Eocene Thermal Maximum warming, Nat. Geosci., 2(8), 576–580. doi:10.1038/ngeo578.

Ziegler, A. M., Eshel, G., Rees, P. M., Rothfus, T. A., Rowley, D. B., Sunderlin, D., 2003. Tracing the tropics across land and sea: Permian to present. Lethaia 36, 227-254.

Figures:

Figure 1. Paleogeography at the Paleocene-Eocene boundary, ~55 Ma. Adapted from Ocean Drilling Stratigraphic Network (ODSN) Paleomap project (http://www.odsn.de/odsn/services/paleomap/paleomap.html).

Figure 2. ODP Site 1262 bulk and benthic stable isotope, %CF and Fe area data (re)plotted against age (solution 1, Westerhold et al., 2008, updated for the post ETM-2 period). Bulk $\delta^{13}C$ data from Lourens et al., 2005; Zachos et al., 2005, 2010; PETM benthic stable isotope data from McCarren et al., 2008; ETM benthic stable isotope data from Stap et al., 2010; Fe data from Westerhold et al., 2007. To the left of the dashed grey line is the benthic stable isotope and %CF data generated at UCSC (except for ETM-2), and to the right is the data

1045 generated at MARUM. See Supplementary Information Fig. S1 for all data plotted against
1046 depth.
1047
1048 **Figure 3**. Band pass filters for the detrended, linearly interpolated, orbitally-tuned benthic
1049 carbon-isotope (red) and oxygen-isotope (blue) records, for principal orbital frequencies:
1050 long and short eccentricity (405 (0.0024 ± 0.0007); 100 kyr (0.01 ± 0.003)) and precession
1051 (21 kyr (0.0476 ± 0.0143)). "W" numbers at base of figure indicate windows of time
1052 referred to in Figs. S6–7.
1053
1054 **Figure 4.** Multi-Taper Method (MTM) power spectrum for the Site 1262 benthic isotope
1055 and %CF records, 52.5–60.6 Ma.
1056
1057 **Figure 5.** Wavelet analysis of Site 1262 data. A) %CF data, B) benthic $\delta^{18}O$ data, C) benthic
1058 $\delta^{13}C$ data.
1059
1060 **Figure 6**. Blackman-Tukey cross-spectral phase estimates, coherence and phasing, between
1061 (**A**) benthic oxygen- and carbon-isotope records, and (B) %CF and benthic carbon-isotope
1062 records, for the entire Site 1262 record, (52.5–60.6 Ma). Cross-spectral phase estimates for
1063 discrete windows of Eocene and Paleocene time are shown in Figs. S6–S7.
1064
1065 **Figure 7**. Site 1262 (Atlantic) vs. Site 1209 (Pacific; Westerhold et al., 2011) benthic
1066 isotope, sedimentation rate, and %CF data plotted against the same age model (Solution 1,
1067 Westerhold et al., (2008), updated for the post ETM-2 period).

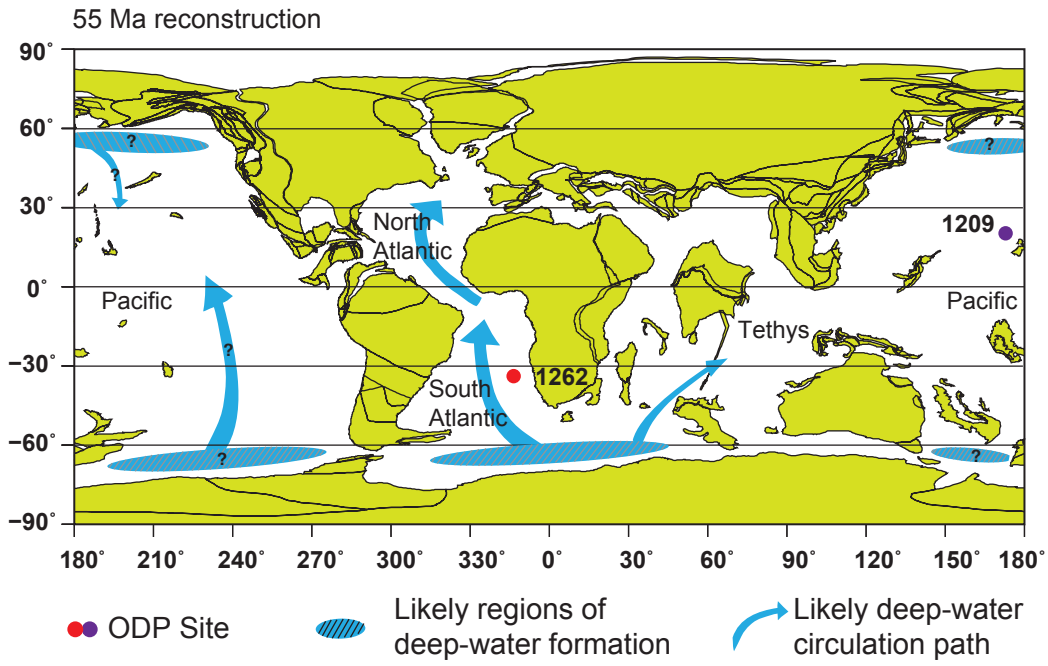
55 Ma reconstruction
90˚
60˚
30˚
0˚
−30˚
−60˚
−90˚
180˚
210˚
240˚
270˚
300˚
330˚
0˚
30˚
60˚
90˚
120˚
150˚
180˚
North Atlantic
South Atlantic
Pacific
Pacific
Tethys
1209
1262
?
ODP Site
Likely regions of deep-water formation
Likely deep-water circulation path

Figure 1.

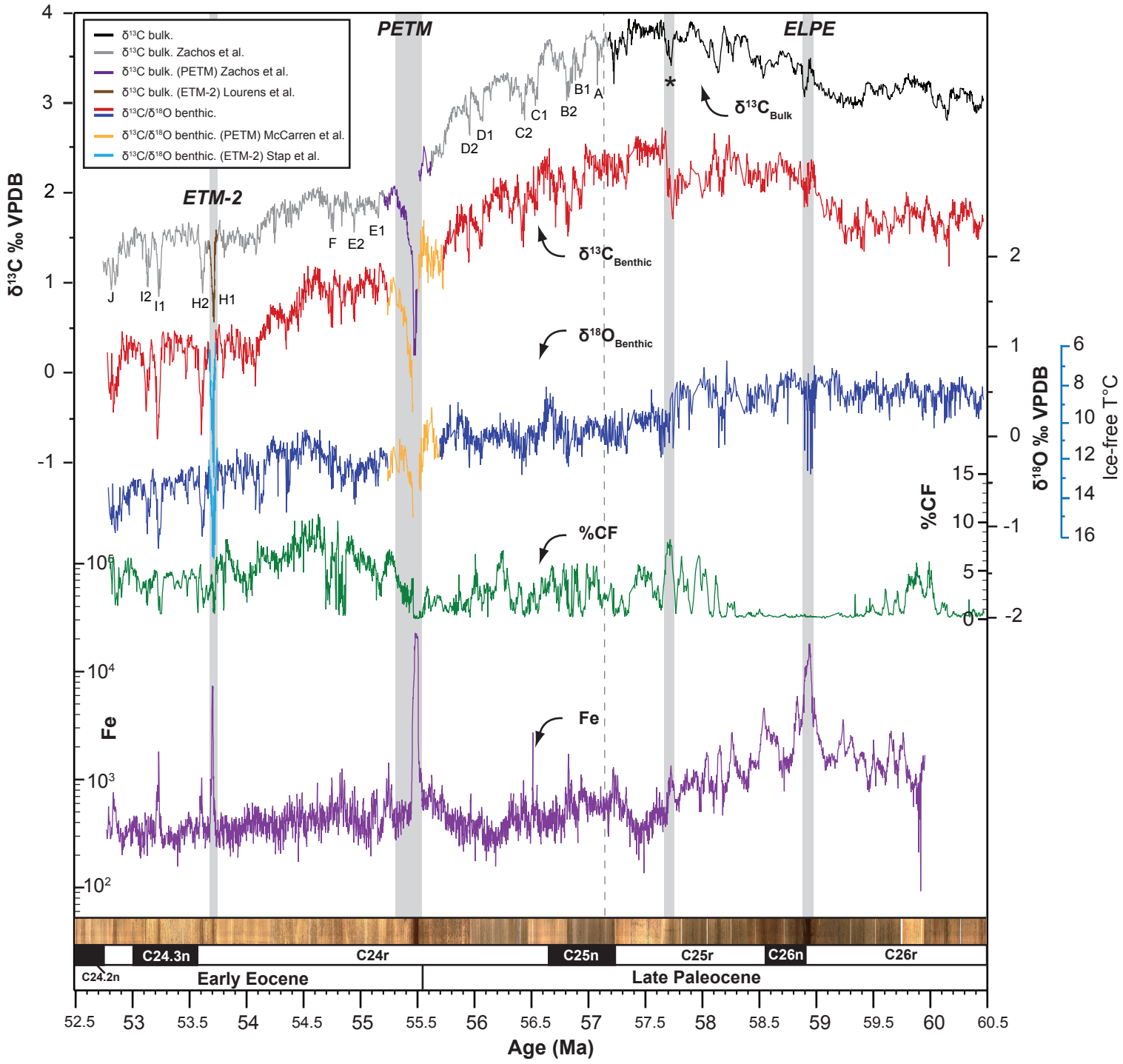
δ13C bulk.
δ13C bulk. Zachos et al.
δ13C bulk. (PETM) Zachos et al.
δ13C bulk. (ETM-2) Lourens et al.
δ13C/δ18O benthic.
δ13C/δ18O benthic. (PETM) McCarren et al.
δ13C/δ18O benthic. (ETM-2) Stap et al.
PETM
ELPE
ETM-2
δ13CBulk
δ13CBenthic
δ18OBenthic
%CF
Fe
δ13C ‰ VPDB
δ18O ‰ VPDB
Ice-free T°C
Age (Ma)
C24.2n
C24.3n
C24r
C25n
C25r
C26n
C26r
Early Eocene
Late Paleocene

Figure 2.

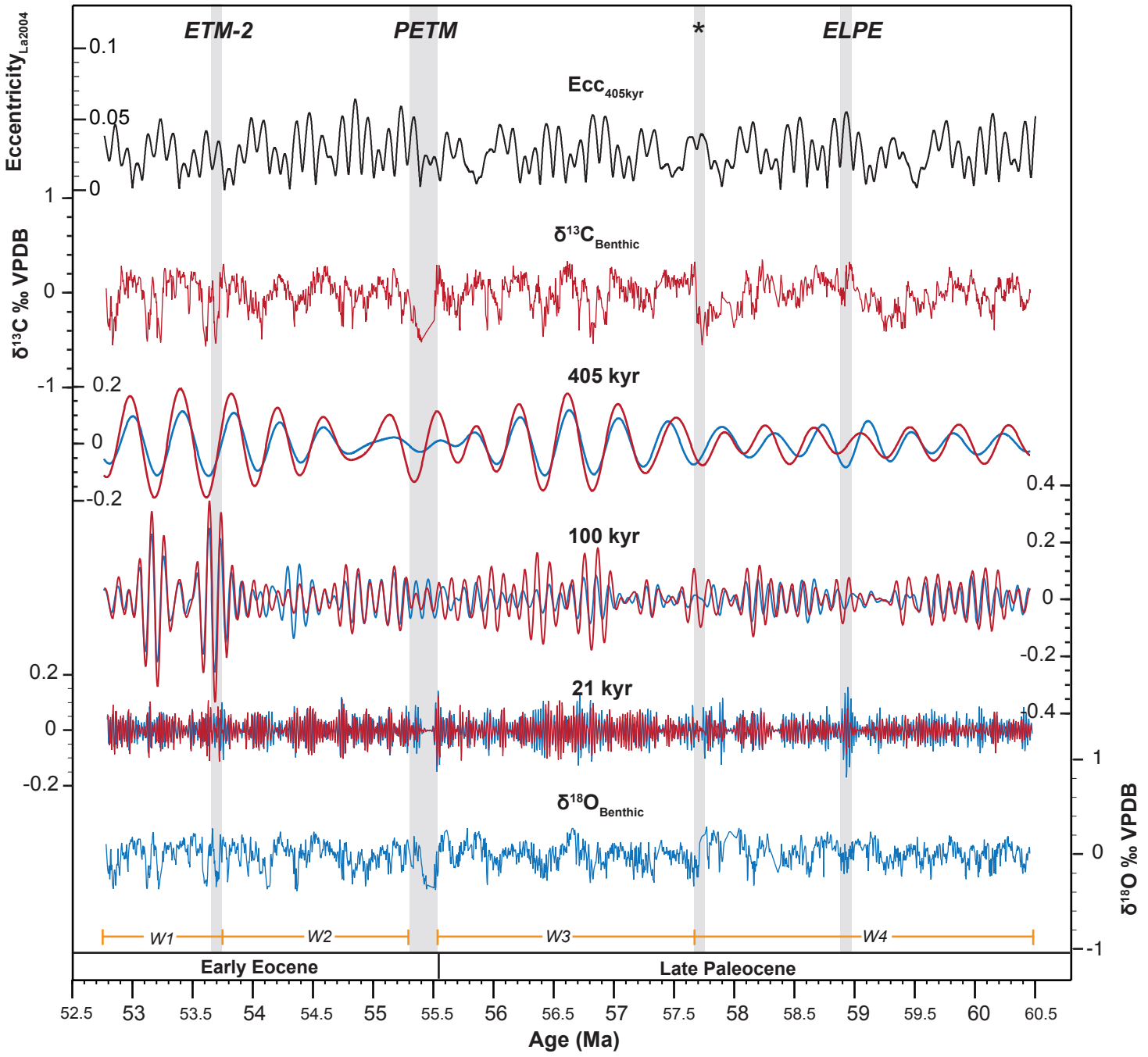
ETM-2
PETM
*
ELPE
Eccentricity La2004
Ecc 405kyr
δ13C ‰ VPDB
δ13C Benthic
405 kyr
100 kyr
21 kyr
δ18O Benthic
δ18O ‰ VPDB
W1
W2
W3
W4
Early Eocene
Late Paleocene
Age (Ma)

Figure 3.

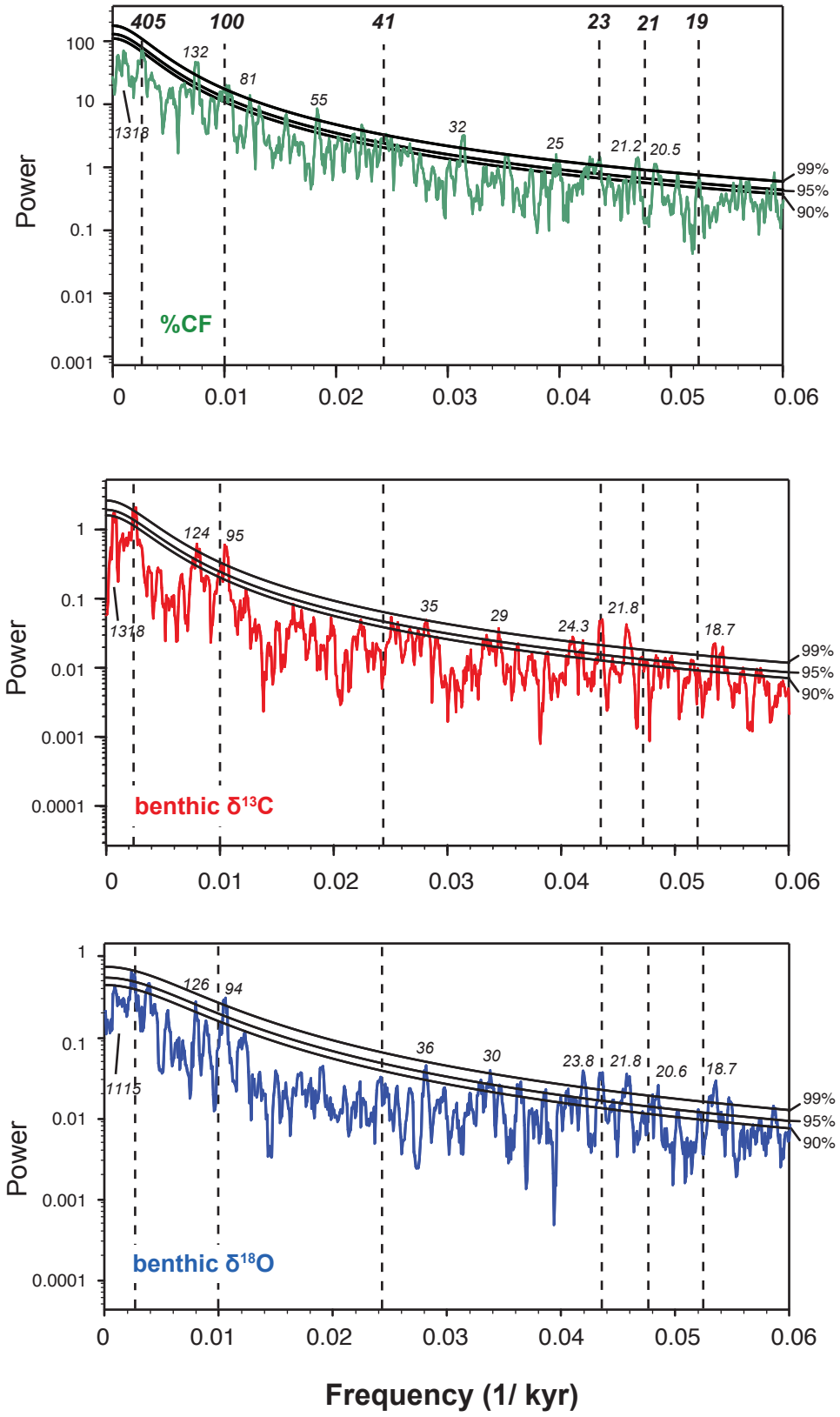
405
100
41
23
21
19
132
81
55
32
25
21.2
20.5
1318
99%
95%
90%
Power
%CF
124
95
35
29
24.3
21.8
18.7
benthic δ13C
126
94
36
30
23.8
21.8
20.6
18.7
1115
benthic δ18O
Frequency (1/ kyr)

Figure 4.

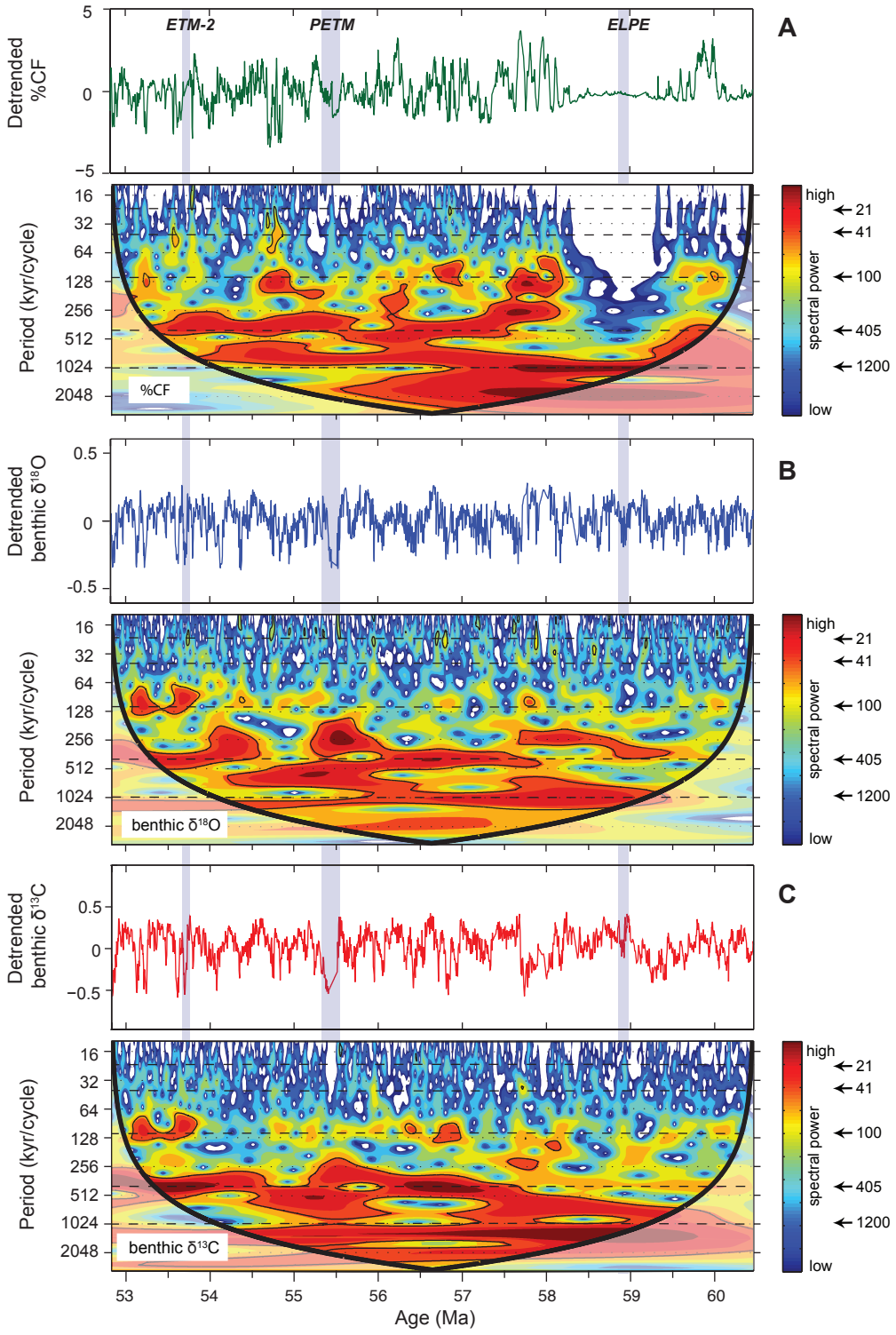
ETM-2
PETM
ELPE
A
Detrended %CF
5
0
−5
Period (kyr/cycle)
16
32
64
128
256
512
1024
2048
%CF
high
spectral power
low
21
41
100
405
1200
B
Detrended benthic δ18O
0.5
0
-0.5
benthic δ18O
C
Detrended benthic δ13C
0.5
0
−0.5
benthic δ13C
53
54
55
56
57
58
59
60
Age (Ma)

Figure 5.

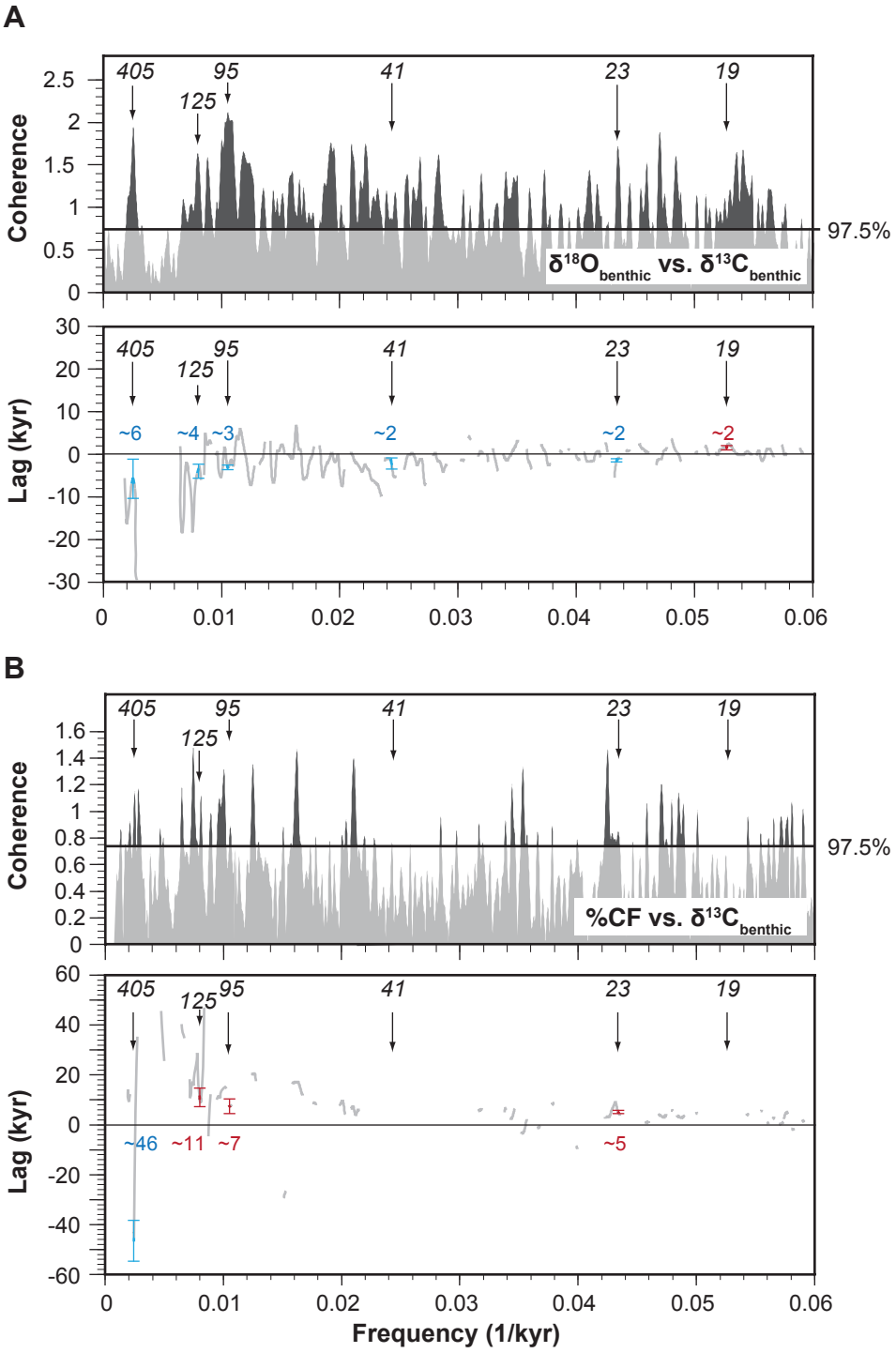
A
405
95
125
41
23
19
Coherence
2.5
2
1.5
1
0.5
0
97.5%
δ18Obenthic vs. δ13Cbenthic
Lag (kyr)
30
20
10
0
-10
-20
-30
~6
~4
~3
~2
~2
~2
0
0.01
0.02
0.03
0.04
0.05
0.06
B
405
95
125
41
23
19
Coherence
1.6
1.4
1.2
1
0.8
0.6
0.4
0.2
0
97.5%
%CF vs. δ13Cbenthic
Lag (kyr)
60
40
20
0
-20
-40
-60
~46
~11
~7
~5
0
0.01
0.02
0.03
0.04
0.05
0.06
Frequency (1/kyr)

Figure 6.

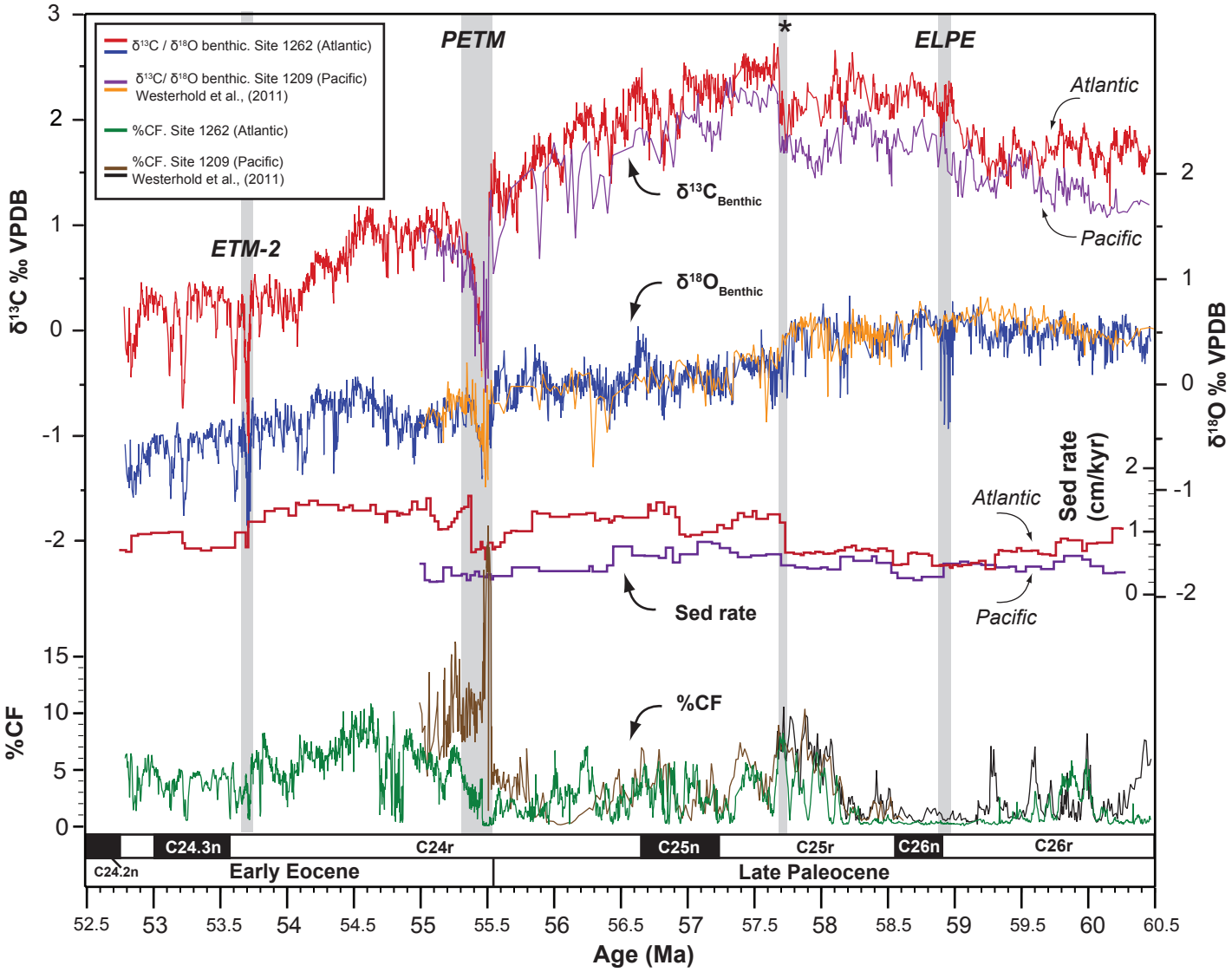
δ13C / δ18O benthic. Site 1262 (Atlantic)
δ13C/ δ18O benthic. Site 1209 (Pacific) Westerhold et al., (2011)
%CF. Site 1262 (Atlantic)
%CF. Site 1209 (Pacific) Westerhold et al., (2011)
PETM
ELPE
ETM-2
*
Atlantic
Pacific
δ13CBenthic
δ18OBenthic
Sed rate
Sed rate (cm/kyr)
%CF
δ13C ‰ VPDB
δ18O ‰ VPDB
C24.2n
C24.3n
C24r
C25n
C25r
C26n
C26r
Early Eocene
Late Paleocene
Age (Ma)

Figure 7.

A high-resolution benthic stable-isotope record for the South Atlantic: implications for orbital-scale changes in Late Paleocene–Early Eocene climate and carbon cycling

Kate Littler; Ursula Röhl; Thomas Westerhold; James C. Zachos

Supplementary Information

Supplementary figures:

Fig. S1. All isotope and %CF data from Site 1262 plotted against depth (mcd).

Fig. S2. Paleocene isotopic and %CF data from the Atlantic and Pacific, for A) the Mid -PCIM event, and B) the ELPE event.

Fig. S3. Benthic stable isotope data from the Eocene at ODP Site 1262.

Fig. S4. All oxygen-isotope data from ODP Site 1262 plotted against age.

Fig. S5. Benthic stable-isotope and %CF data from the Late Paleocene at Site 1262 plotted against age, showing the prominent eccentricity-paced variation.

Fig. S6. Blackman-Tukey cross-spectral phase estimates, coherance and phasing, between oxygen- and carbon-isotope records for four discrete windows of time.

Fig. S7. Blackman-Tukey cross-spectral phase estimates, coherance and phasing, between %CF and carbon-isotope records for four discrete windows of time.

Tables S1 & S2. Coherency and phasing data for both the entire record and discrete windows of time, at key orbital frequencies.

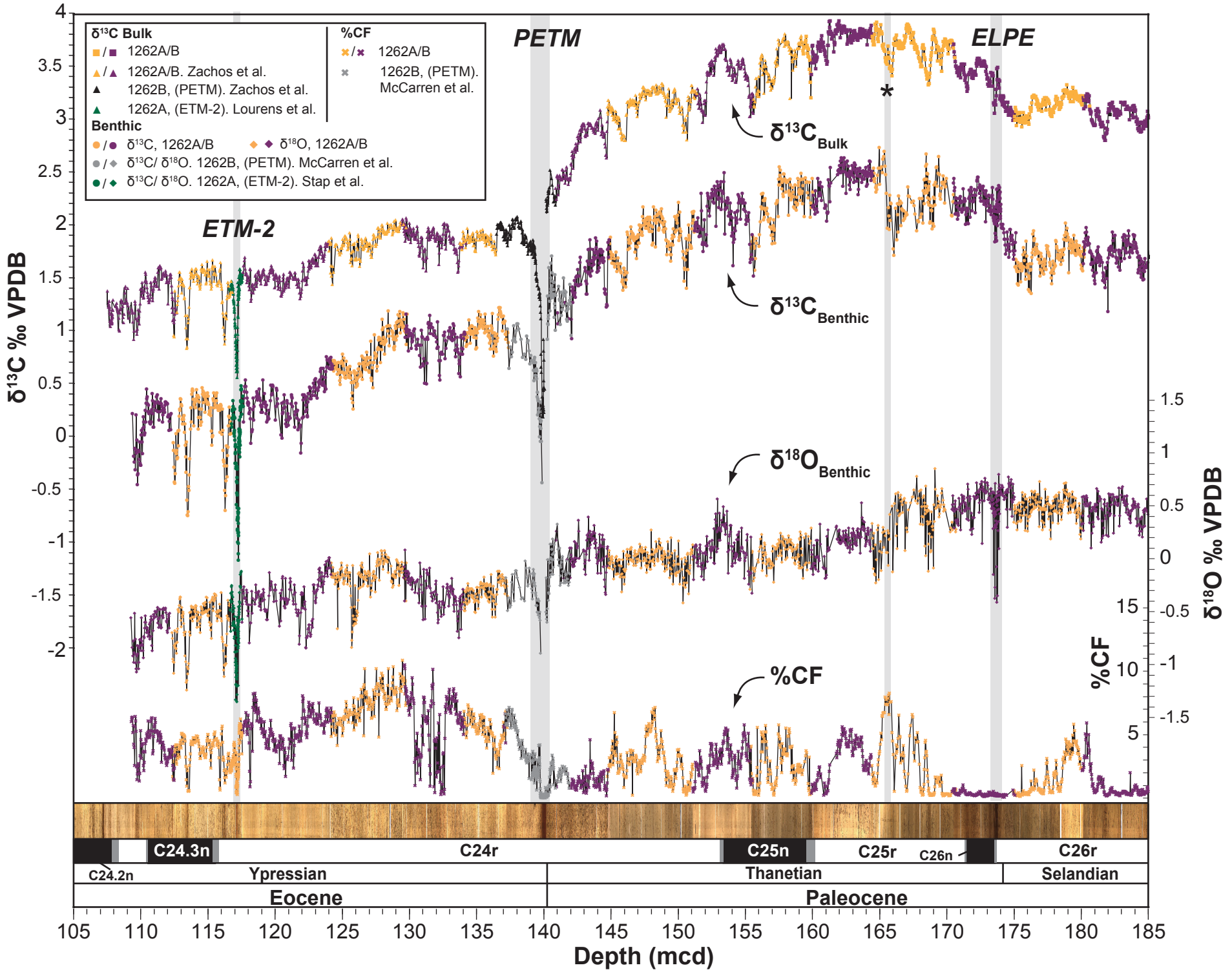

Figure S1. All isotope and %CF data from Site 1262 plotted against depth (mcd).

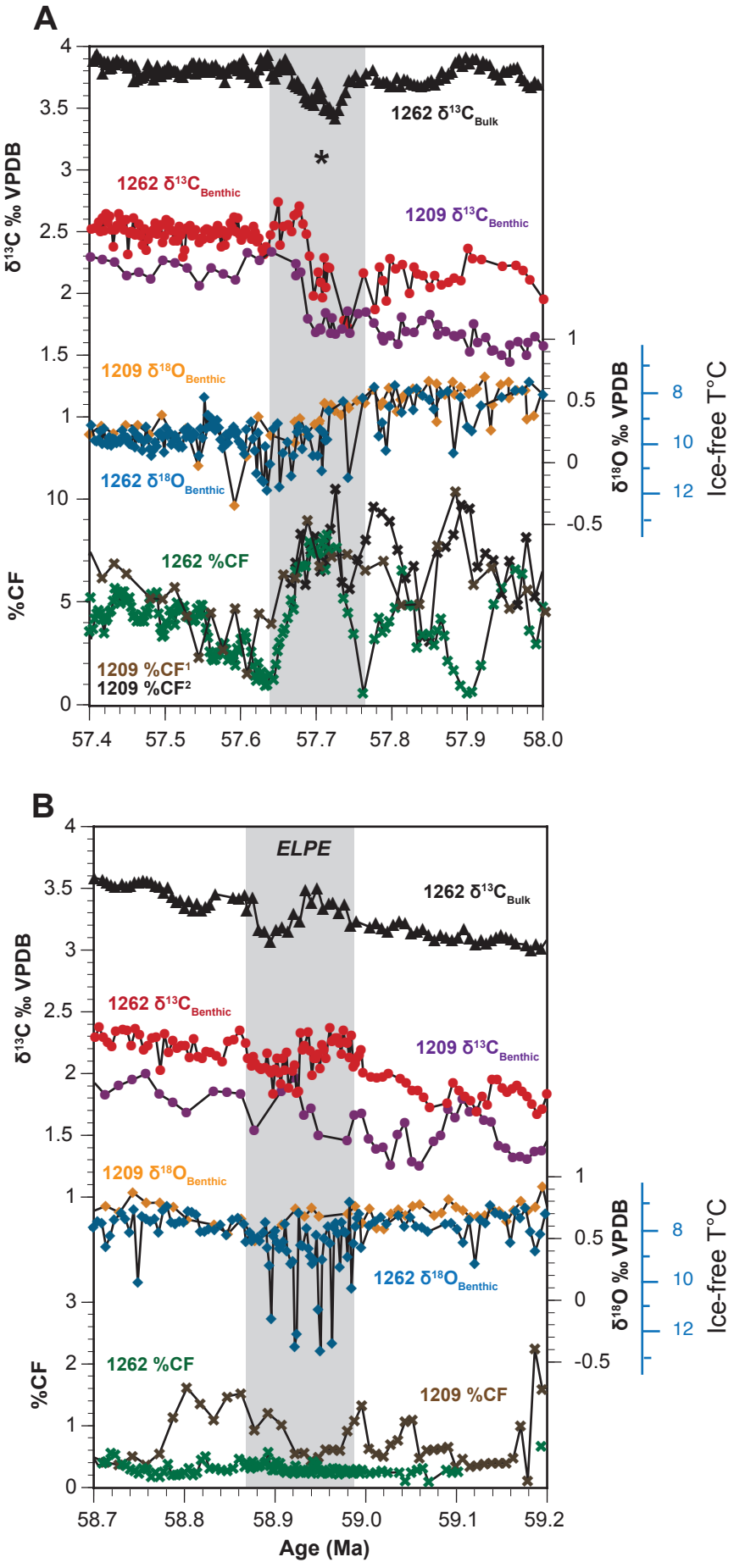

Figure S2. Paleocene isotopic and %CF data from Site 1262 (Atlantic) and Site 1209 (Pacific; Westerhold et al., 2011) for: A) 58.7–59.2 ma, the "peak-PCIM" event near the middle of Chron C25r; and B) 57.4–58 Ma, the ELPE event. At Site 1209, %CF[1] (brown)= >63 µm; %CF[2] (black) = >38 µm fraction.

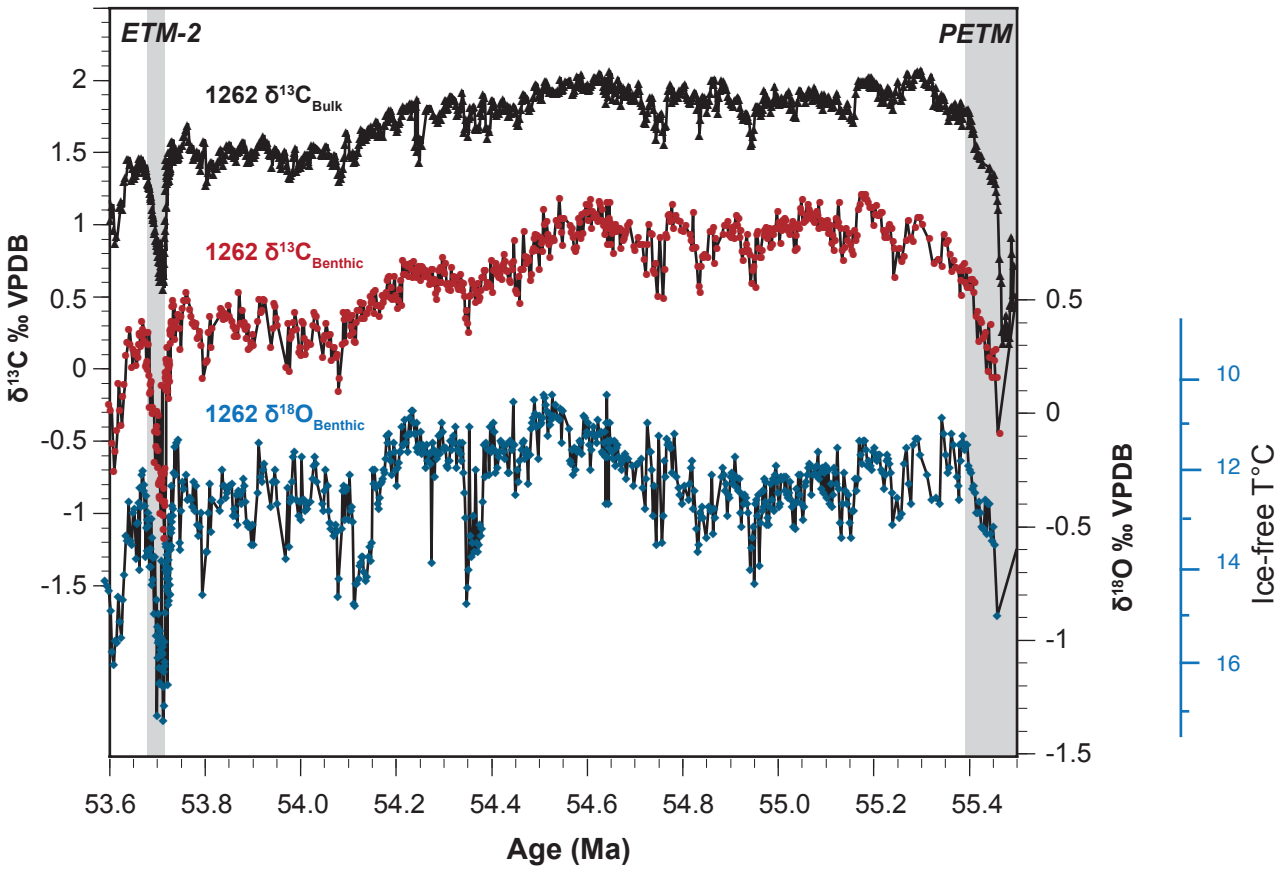

Figure S3. Benthic stable isotope data from the Eocene at Site 1262 showing cooling reversal at 54.5–54.9 Ma, and reestablishment of the negative trend in carbon isotopes at ~54.6 Ma.

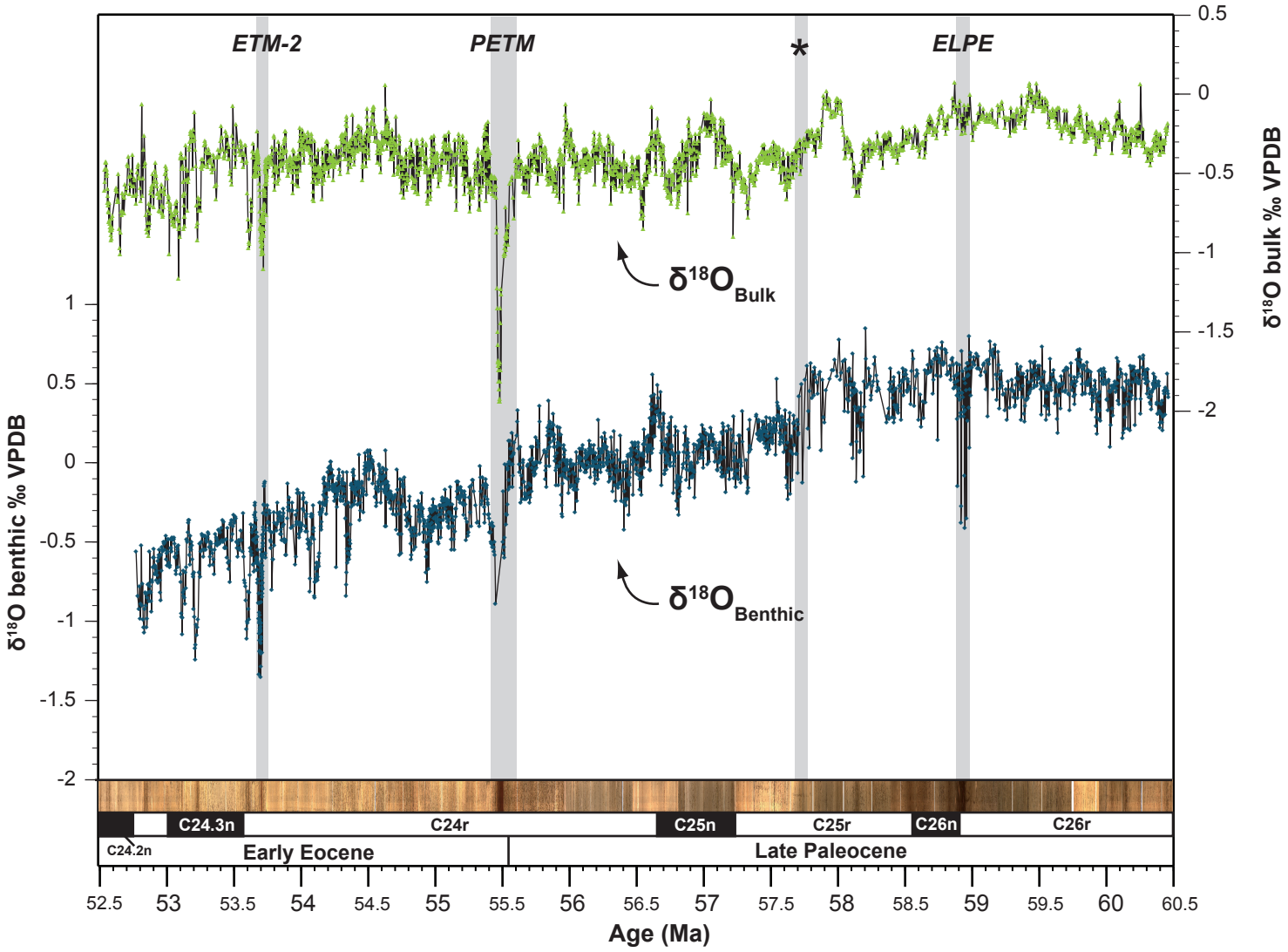

Figure S4. All oxygen-isotope data, benthic (this study) and bulk (Zachos et al., 2010), from ODP Site 1262 plotted against age

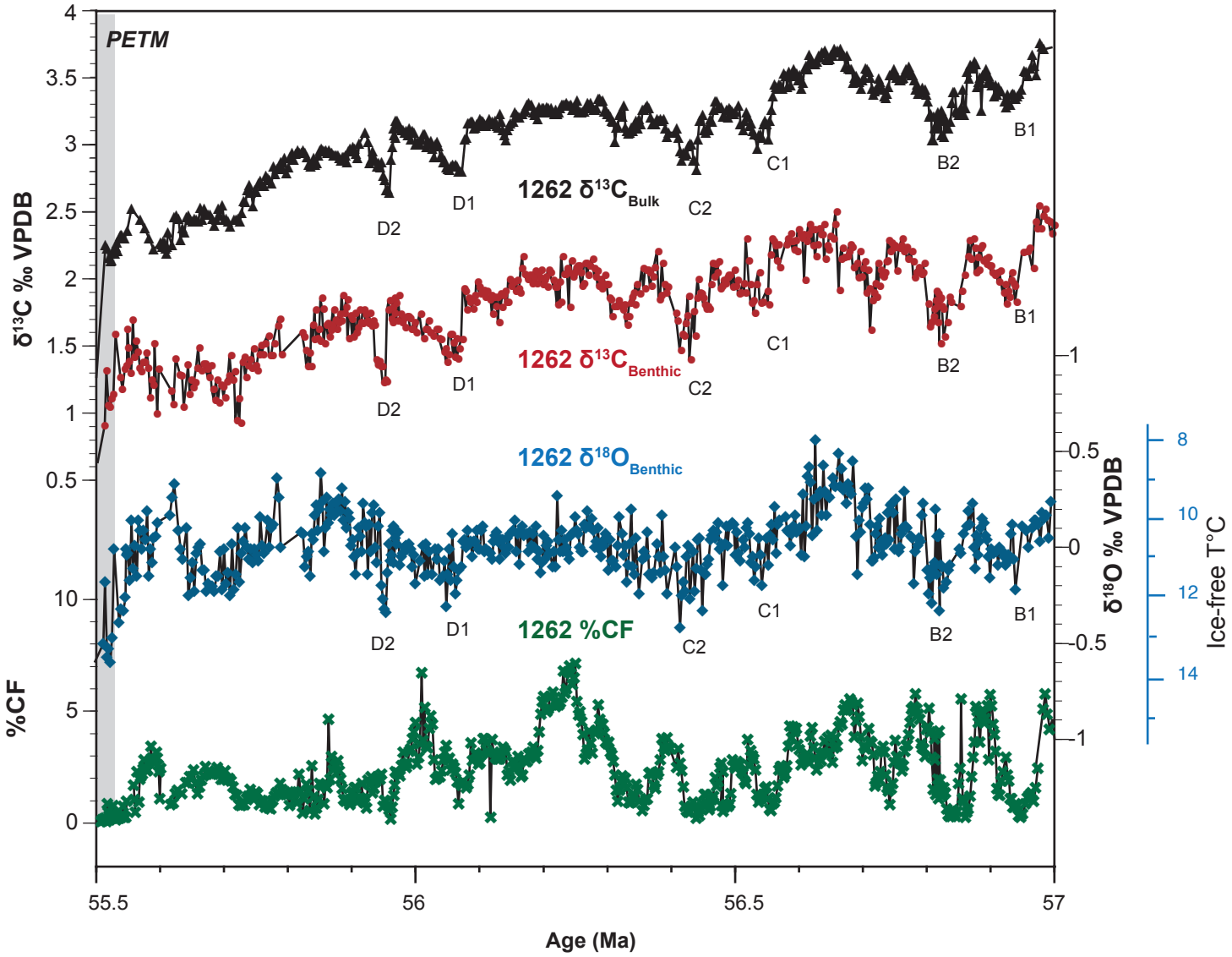

Figure S5. Benthic stable-isotope and %CF data from the Late Paleocene at Site 1262 plotted against age, showing the prominent eccentricity-paced variation. Close covariation on orbital timescales between both $\delta^{18}O$ and $\delta^{13}C$, and isotopic records and %CF, is clearly visible. Changes in bottom water temperature of ~4°C from the large C2 to B2 405 kyr, and changes of ~1.5°C associated with the larger 100-kyr paced events such as D2, can be seen in the benthic $\delta^{18}O$ record.

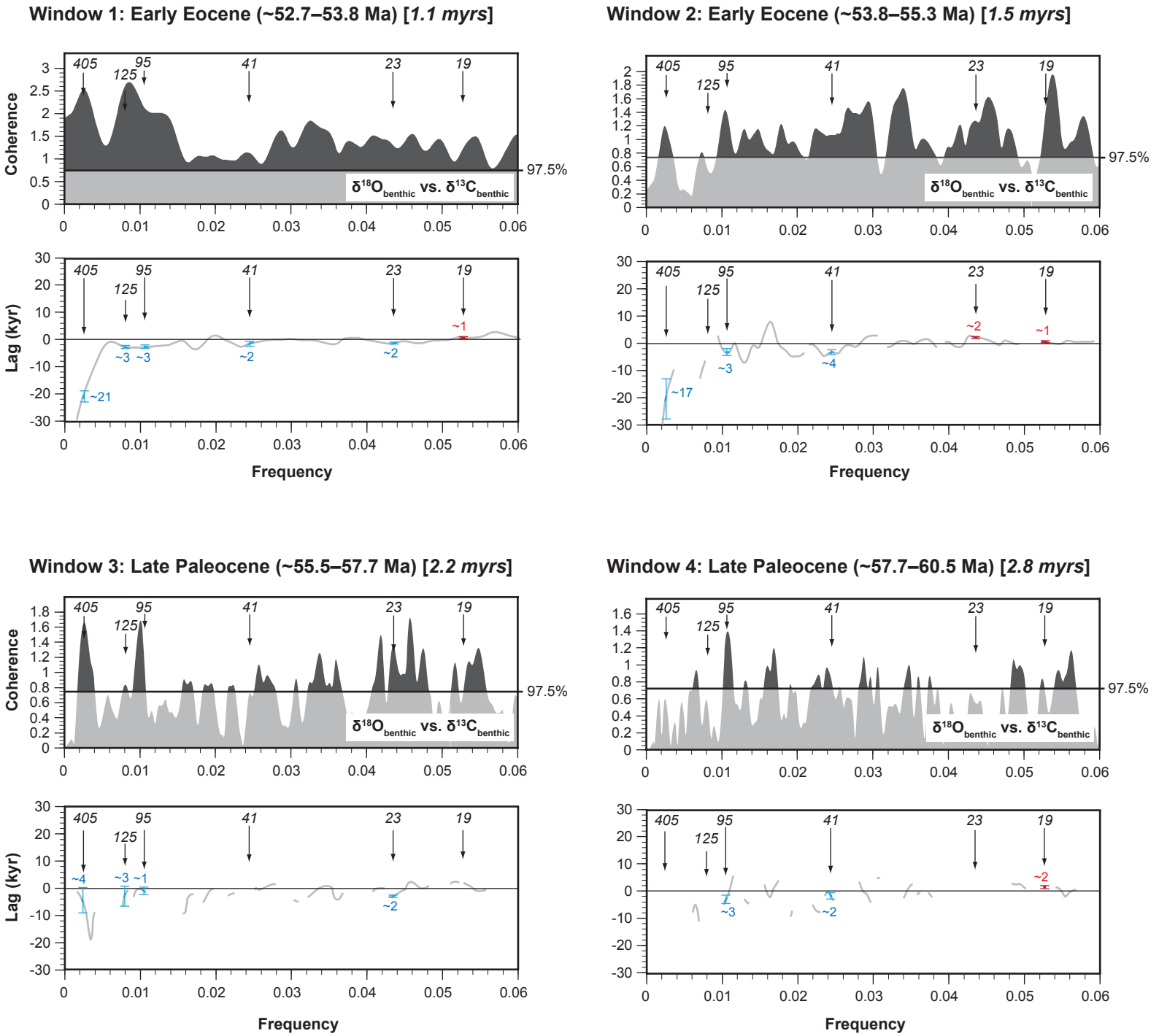

Figure S6. Blackman-Tukey cross-spectral phase estimates, coherance and phasing, between oxygen- and carbon-isotope records for four discrete windows of time (Window 1 and 2: Eocene; Window 3 and 4: Paleocene). See Fig. 6 for cross-spectral phase estimates for the entire record. See Fig. 3 for the location of the “W” windows relative to the stable-isotope records.

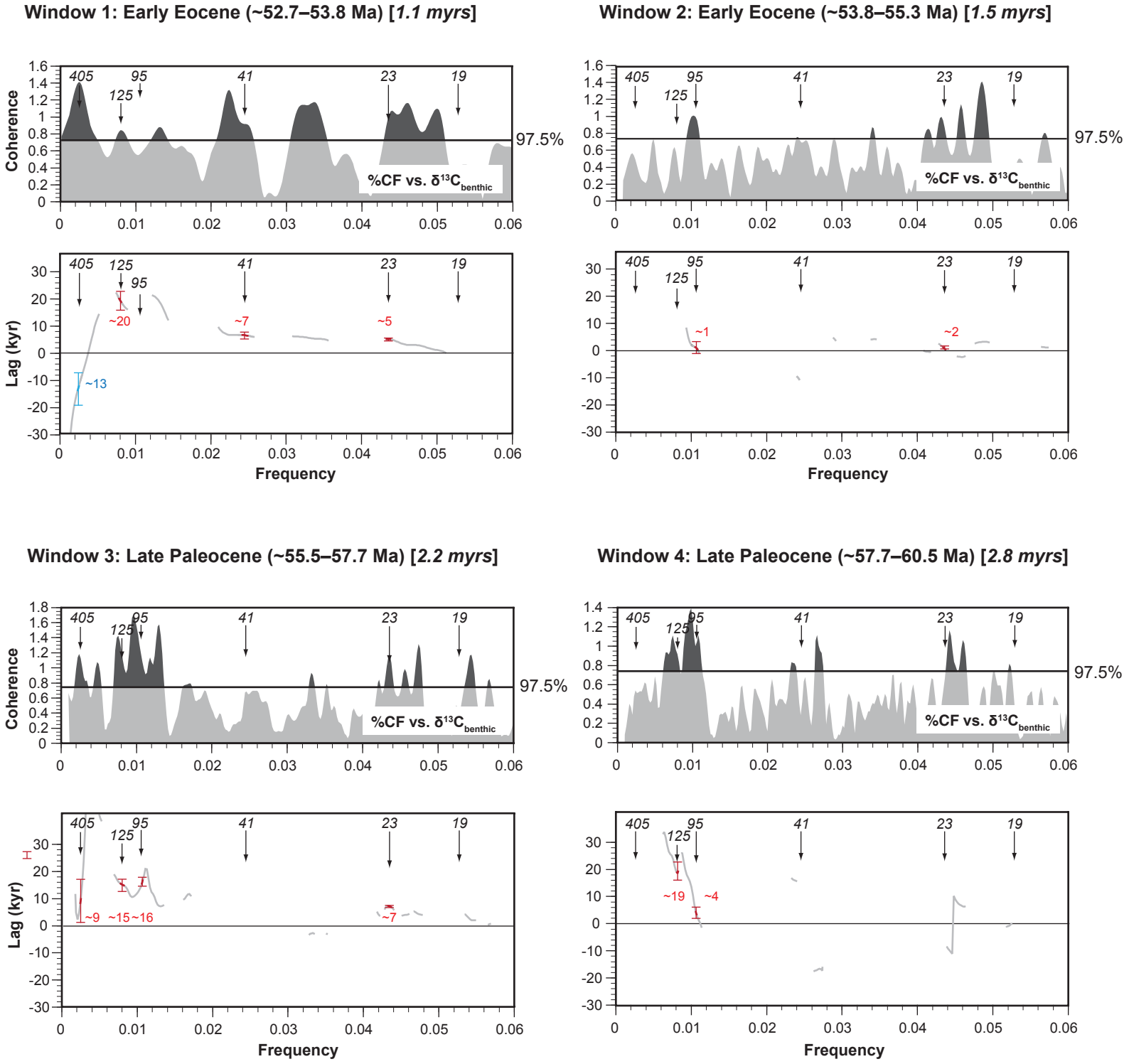

Figure S7. .Blackman-Tukey cross-spectral phase estimates, coherance and phasing, between %CF and carbon-isotope records for four discrete windows of time (Window 1 and 2: Eocene; Window 3 and 4: Paleocene). See Fig. 6 for cross-spectral phase estimates for the entire record. See Fig. 3 for the location of the "W" windows relative to the stable-isotope records.

Whole record: $\delta^{13}C$ benthic vs. $\delta^{18}O$ benthic

Orbital frequency	Frequency	Coherency (0.672031)	Lag (kyr)	Max Lag (kyr)	Min Lag (kyr)
405 kyr	0.00247	1.79692	-5.65	-10.41	-0.88
125 kyr	0.008	1.63440	-3.95	-5.69	-2.20
95 kyr	0.01053	2.11371	-3.16	-3.96	-2.37
41 kyr	0.02439	0.87359	-2.24	-3.67	-0.81
23 kyrs	0.0434	1.44640	-1.49	-1.89	-1.10
19 kyrs	0.0526	1.09178	1.55	1.05	2.04

Whole record: %CF vs. $\delta^{13}C$ benthic

Orbital frequency	Frequency	Coherency (0.737575)	Lag (kyr)	Max Lag (kyr)	Min Lag (kyr)
405 kyr	0.00247	1.12209	-46.53	-54.76	-38.30
125 kyr	0.008	0.86335	10.89	7.33	14.46
95 kyr	0.01053	0.83449	7.36	4.53	10.19
41 kyr	0.02439	0.35757	-6.95	-10.10	-3.80
23 kyrs	0.0434	0.84733	5.03	4.36	5.70
19 kyrs	0.0526	0.50024	-5.11	-6.13	-4.09

Table S1. Coherency and phasing data for the entire 7.7 myr long record at key orbital frequencies generated using Analyseries Blackman-Tukey cross-spectral analysis. Values in brackets represent the threshold coherency value at the 97.5% CI. Data is plotted in Fig. 6.

Window 1, Eocene: δ^{13}C benthic vs. δ^{18}O benthic

Orbital frequency	Frequency	Coherency (0.738192)	Lag (kyr)	Max Lag (kyr)	Min Lag (kyr)
405 kyr	0.00247	2.51818	-21.09	-22.97	-19.21
125 kyr	0.0080	2.59823	-2.78	-3.30	-2.26
95 kyr	0.01053	2.13554	-2.83	-3.46	-2.20
41 kyr	0.02439	1.13939	-1.65	-2.46	-0.84
23 kyrs	0.0434	1.32461	-1.49	-1.85	-1.12
19 kyrs	0.0526	1.17498	0.72	0.36	1.08

Window 2, Eocene: δ^{13}C benthic vs. δ^{18}O benthic

Orbital frequency	Frequency	Coherency (0.737782)	Lag (kyr)	Max Lag (kyr)	Min Lag (kyr)
405 kyr	0.00247	1.19518	-20.62	-28.03	-13.22
125 kyr	0.0080	0.60841	-4.72	-10.11	0.66
95 kyr	0.01053	1.43375	-3.35	-4.69	-2.01
41 kyr	0.02439	1.06917	-3.33	-4.22	-2.44
23 kyrs	0.0434	1.27101	2.24	1.85	2.63
19 kyrs	0.0526	1.13821	0.53	0.15	0.90

Window 3, Paleocene: δ^{13}C benthic vs. δ^{18}O benthic

Orbital frequency	Frequency	Coherency (0.742183)	Lag (kyr)	Max Lag (kyr)	Min Lag (kyr)
405 kyr	0.00247	1.60522	-4.40	-9.24	0.44
125 kyr	0.0080	0.83422	-2.78	-6.50	0.93
95 kyr	0.01053	1.32471	-1.04	-2.55	0.48
41 kyr	0.02439	0.68875	-0.48	-2.01	1.05
23 kyrs	0.0434	1.33064	-2.93	-3.29	-2.56
19 kyrs	0.0526	0.61719	2.45	1.65	3.26

Window 4, Paleocene: δ^{13}C benthic vs. δ^{18}O benthic

Orbital frequency	Frequency	Coherency (0.737908)	Lag (kyr)	Max Lag (kyr)	Min Lag (kyr)
405 kyr	0.00247	0.58444	-15.61	-34.39	3.17
125 kyr	0.008	0.58818	-3.20	-8.79	2.40
95 kyr	0.01053	1.296218638	-2.98	-4.55	-1.42
41 kyr	0.02439	0.86213	-1.75	-2.92	-0.57
23 kyrs	0.0434	0.57708	0.32	-0.73	1.38
19 kyrs	0.0526	0.80043	1.41	0.81	2.00

Table S2a. Coherency and phasing data for discrete windows of time at key orbital frequencies, for δ^{13}C benthic vs. δ^{18}O benthic data, generated using Analyseries Blackman-Tukey cross-spectral analysis. Values in brackets represent the threshold coherency value at the 97.5% CI. Data is plotted in Fig. S6.

Window 1, Eocene: %CF vs. δ^{13}C benthic

Orbital frequency	Frequency	Coherency (0.729578)	Lag (kyr)	Max Lag (kyr)	Min Lag (kyr)
405 kyr	0.00247	1.41084	-13.04	-19.06	-7.03
125 kyr	0.008	0.84286	19.54	15.86	23.22
95 kyr	0.01053	0.56364	19.89	15.46	24.32
41 kyr	0.02439	0.91913	6.73	5.64	7.81
23 kyrs	0.0434	0.96693	5.23	4.66	5.80
19 kyrs	0.0526	0.39143	-4.00	-5.33	-2.67

Window 2, Eocene: %CF vs. δ^{13}C benthic

Orbital frequency	Frequency	Coherency (0.737782)	Lag (kyr)	Max Lag (kyr)	Min Lag (kyr)
405 kyr	0.00247	0.53979	-51.30	-71.81	-30.78
125 kyr	0.008	0.57941	-15.39	-21.08	-9.70
95 kyr	0.01053	0.99597	1.14	-1.11	3.38
41 kyr	0.02439	0.71854	-10.79	-12.25	-9.33
23 kyrs	0.0434	0.95438	1.23	0.65	1.81
19 kyrs	0.0526	0.20967	-5.77	-8.35	-3.19

Window 3, Paleocene: %CF vs. δ^{13}C benthic

Orbital frequency	Frequency	Coherency (0.737840)	Lag (kyr)	Max Lag (kyr)	Min Lag (kyr)
405 kyr	0.00247	1.18552	9.16	1.35	16.96
125 kyr	0.008	1.23248	14.92	12.70	17.13
95 kyr	0.01053	1.19673	16.25	14.51	18.00
41 kyr	0.02439	0.67453	2.68	1.11	4.25
23 kyrs	0.0434	1.14395	7.12	6.67	7.58
19 kyrs	0.0526	0.47913	0.49	-0.58	1.55

Window 4, Paleocene: %CF vs. δ^{13}C benthic

Orbital frequency	Frequency	Coherency (0.737908)	Lag (kyr)	Max Lag (kyr)	Min Lag (kyr)
405 kyr	0.00247	0.54238	64.94	44.54	85.35
125 kyr	0.008	0.91532	19.34	16.02	22.65
95 kyr	0.01053	1.04355	3.99	1.88	6.10
41 kyr	0.02439	0.28302	18.23	14.20	22.26
23 kyrs	0.0434	0.54647	-8.39	-9.50	-7.27
19 kyrs	0.0526	0.66113	0.06	-0.68	0.81

Table S2b. Coherency and phasing data for discrete windows of time at key orbital frequencies, for %CF vs. δ^{13}C benthic data, generated using Analyseries Blackman-Tukey cross-spectral analysis. Values in brackets represent the threshold coherency value at the 97.5% CI. Data is plotted in Fig. S7.